The Astrophysical Journal, 858:95 (22pp), 2018 May 10 https://doi.org/10.3847/1538-4357/aab6ad

Electron Heating in Low Mach Number Perpendicular Shocks. II. Dependence on the Pre-shock Conditions

Xinyi Guo[1], Lorenzo Sironi[2], and Ramesh Narayan[1]
[1] Harvard-Smithsonian Center for Astrophysics, 60 Garden Street, Cambridge, MA 02138, USA; xinyi.guo@cfa.harvard.edu, rnarayan@cfa.harvard.edu
[2] Department of Astronomy, Columbia University, 550 W 120th Street, New York, NY 10027, USA; lsironi@astro.columbia.edu
Received 2017 December 7; revised 2018 March 6; accepted 2018 March 12; published 2018 May 10

Abstract

Recent X-ray observations of merger shocks in galaxy clusters have shown that the post-shock plasma is two-temperature, with the protons being hotter than the electrons. In this work, the second of a series, we investigate the efficiency of irreversible electron heating in perpendicular low Mach number shocks, by means of two-dimensional particle-in-cell simulations. We consider values of plasma beta (the ratio of thermal and magnetic pressures) in the range $4 \lesssim \beta_{p0} \lesssim 32$, and sonic Mach number (the ratio of shock speed to pre-shock sound speed) in the range $2 \lesssim M_s \lesssim 5$, as appropriate for galaxy cluster shocks. As shown in Paper I, magnetic field amplification—induced by shock compression of the pre-shock field, or by strong proton cyclotron and mirror modes accompanying the relaxation of proton temperature anisotropy—can drive the electron temperature anisotropy beyond the threshold of the electron whistler instability. The growth of whistler waves breaks the electron adiabatic invariance, and allows for efficient entropy production. We find that the post-shock electron temperature T_{e2} exceeds the adiabatic expectation $T_{e2,\rm ad}$ by an amount $(T_{e2} - T_{e2,\rm ad})/T_{e0} \simeq 0.044\, M_s(M_s - 1)$ (here, T_{e0} is the pre-shock temperature), which depends only weakly on the plasma beta over the range $4 \lesssim \beta_{p0} \lesssim 32$ that we have explored, as well as on the proton-to-electron mass ratio (the coefficient of $\simeq$0.044 is measured for our fiducial $m_i/m_e = 49$, and we estimate that it will decrease to $\simeq$0.03 for the realistic mass ratio). Our results have important implications for current and future observations of galaxy cluster shocks in the radio band (synchrotron emission and Sunyaev–Zel'dovich effect) and at X-ray frequencies.

Key words: galaxies: clusters: general – instabilities – radiation mechanisms: thermal – shock waves

1. Introduction

Cluster merger shocks—collisionless low Mach number shocks ($M_s \lesssim 5$, where M_s is the ratio of shock speed to pre-shock sound speed) generated by infalling subclusters—are routinely observed in the radio and X-ray bands. X-ray measurements can quantify the density and temperature jumps between the unshocked (upstream) and the shocked (downstream) plasma (e.g., Markevitch et al. 2002; Finoguenov et al. 2010; Russell et al. 2010; Ogrean et al. 2013; Eckert et al. 2016; Akamatsu et al. 2017). The existence of shock-accelerated electrons is revealed by radio observations of synchrotron radiation (e.g., van Weeren et al. 2010; Lindner et al. 2014; Trasatti et al. 2015; Kale et al. 2017). Recently, the pressure jump associated with a merger shock has been measured through radio observations of the thermal Sunyaev–Zel'dovich (SZ) effect (Planck Collaboration et al. 2013; Erler et al. 2015; Basu et al. 2016).

Because all observational diagnostics are based on radiation emitted by electrons, the proton properties (in particular, their temperature) are basically unconstrained. One usually makes the simplifying assumption that the electron temperature equals the proton temperature (and so, the mean gas temperature). This assumption is unlikely to hold in the vicinity of merger shocks, because most of the pre-shock energy is carried by protons and there is no obvious reason why protons should efficiently share the thermal energy they gain in passing through the shock with electrons.[3] While Coulomb collisions will eventually drive electrons and protons to equal temperatures, the collisional equilibration timescale (Spitzer 1962) for typical conditions in the intracluster medium (ICM) is as long as 10^8–10^9 years. In fact, X-ray observations by Russell et al. (2012) have shown that the electron temperature just behind a merger shock in Abell 2146 is lower than the mean gas temperature expected from the Rankine–Hugoniot jump conditions, and thus lower than the proton temperature. On the other hand, Markevitch (2006) found that the temperatures across the shock in 1E 0657-56 (the so-called "Bullet cluster") are consistent with instant shock-heating of the electrons.

What is the mechanism responsible for electron heating at collisionless shocks, and how does the heating efficiency depend on the pre-shock conditions? This fundamental question can be answered only through a detailed plasma physics analysis because the fluid-type Rankine–Hugoniot relations only predict the jump in the mean plasma temperature across the shock, without specifying how the shock-generated heat is distributed between the two species. While most of the electron heating in low Mach number shocks is *adiabatic*, the passage of electrons through the shock might also be accompanied by entropy increase, i.e., by the production of *irreversible* electron heating. In the absence of a first-principles theory of electron heating in collisionless shocks, Vink et al. (2015) employed a phenomenological parameter—which was constrained by fitting the observations—in order to quantify the efficiency of irreversible energy transfer from protons to electrons.[4] In this paper, we adopt a different approach. We aim at understanding, on a fundamental level, the role of electron and proton plasma instabilities in particle heating at low Mach number shocks, by means of fully kinetic simulations with the

[3] Shocks in supernova remnants and the heliosphere are known to be two-temperature, with protons hotter than electrons (e.g., Ghavamian et al. 2013).

[4] We caution that, in the model of Vink et al. (2015), the mean (electron +proton) temperature jump does not agree with the expected Rankine–Hugoniot conditions because the authors neglected the conservation of the momentum flux through the shock, but still employed the Rankine–Hugoniot density jump—which implicitly requires momentum conservation—in deriving the post-shock electron-to-proton temperature ratio.

particle-in-cell (PIC) method (Hockney & Eastwood 1981; Birdsall & Langdon 1985).

So far, most PIC studies of electron heating in shocks have focused on the regime of high sonic Mach number ($M_s \gtrsim 10$, where M_s is the ratio of the upstream flow speed relative to the shock to the upstream sound speed) and low plasma beta ($\beta_{p0} \lesssim 1$, where β_{p0} is the ratio of thermal and magnetic pressures) appropriate for supernova remnants (Matsukiyo & Scholer 2003; Matsukiyo 2010; Dieckmann et al. 2012). In the first paper of this series (Guo et al. 2017; hereafter, Paper I), we investigated, by means of analytical theory and two-dimensional (2D) PIC simulations, the physics of electron heating in low Mach number perpendicular shocks; a regime previously unexplored. As we summarize in Section 2, we found, in analogy to the so-called "magnetic pumping" mechanism (Spitzer & Witten 1953; Berger et al. 1958; Borovsky 1986), that two basic ingredients are needed for electron irreversible heating: (i) the presence of a temperature anisotropy, induced by field amplification coupled to adiabatic invariance; and (ii) a mechanism to break the adiabatic invariance. We found that the growth of whistler waves—triggered by the electron temperature anisotropy induced by field amplification—was responsible for the violation of adiabatic invariance and efficient entropy production.

In Paper I, we validated our model for a shock with Mach number $M_s = 3$ and plasma beta $\beta_{p0} = 16$, which we took to be representative of merger shocks in galaxy clusters. In this work, we extend our investigation to a wide range of plasma beta ($4 \lesssim \beta_{p0} \lesssim 32$) and sonic Mach number ($2 \lesssim M_s \lesssim 5$). We quantify how the efficiency of electron heating and the post-shock electron-to-proton temperature ratio depend on M_s and β_{p0}, by means of a suite of 2D simulations. In fact, in Paper I (see their Appendix A) we have shown that the electron heating physics cannot be properly captured by 1D simulations. We focus on perpendicular shocks (i.e., where the pre-shock field is orthogonal to the shock direction of propagation). The choice of a perpendicular magnetic field geometry is meant to minimize the role of non-thermal electrons, which are self-consistently accelerated in oblique configurations, as we have shown in Guo et al. (2014a, 2014b). Because of the absence of shock-accelerated electrons returning upstream, the shock can settle down to a steady state on a shorter time, thus allowing us to focus on the steady-state electron heating physics. However, we expect that the results presented in this paper will also apply to quasi-perpendicular configurations, as long as the non-thermal electrons are energetically sub-dominant.

We find that the dependence on M_s of the electron irreversible heating efficiency can be cast in a simple form: the post-shock electron temperature T_{e2} exceeds the adiabatic expectation $T_{e2,\rm ad}$ by an amount that scales with Mach number as $(T_{e2} - T_{e2,\rm ad})/T_{e0} \simeq 0.044\, M_s(M_s - 1)$, where T_{e0} is the pre-shock temperature. This depends only weakly on plasma beta (in the regime $4 \lesssim \beta_{p0} \lesssim 32$ explored in this work) and on the proton-to-electron mass ratio (which we vary from 49 to 200).

The rest of the paper is organized as follows. In Section 2, we summarize the results of Paper I, where we found that the field amplification required for efficient entropy production can be induced either by shock compression of the upstream field, or by growth of proton cyclotron and mirror modes accompanying the relaxation of proton temperature anisotropy. With periodic box experiments meant to reproduce these two scenarios, Section 3 (Section 4, respectively) investigates the dependence of the electron heating efficiency on Mach number and plasma beta, in a controlled setup where only the first mechanism (the second, respectively) is allowed to operate. Readers primarily interested in the implications of our study for shocks can skip Sections 3 and 4 and proceed directly to Section 5, where we explore how the degree of electron irreversible heating depends on M_s and β_{p0} in full shock simulations (where the two processes discussed above generally co-exist). We present our key findings in Section 6 and conclude with a summary in Section 7.

2. The Physics of Electron Heating

In this section, we summarize the main results of Paper I (see the schematic description in Figure 1). As electrons pass through the shock, they experience a density compression, which results in adiabatic heating. In addition, irreversible processes operate, further increasing the electron temperature. In Paper I, we found that efficient entropy production relies on the presence of two basic ingredients: (i) a temperature anisotropy; and (ii) a mechanism to break adiabatic invariance. The change in electron entropy can then be written in two equivalent forms as:[5]

$$ds_e = \left[\frac{1}{2} d\ln\left(\frac{T_{e,\parallel}}{(n/B)^2}\right)\right]\cdot\left[1 - \frac{T_{e,\parallel}}{T_{e,\perp}}\right] - \frac{de_{w,e}}{T_{e,\perp}}, \quad (1)$$

$$ds_e = -\left[d\ln\left(\frac{T_{e,\perp}}{B}\right)\right]\cdot\left[\frac{T_{e,\perp}}{T_{e,\parallel}} - 1\right] - \frac{de_{w,e}}{T_{e,\parallel}}, \quad (2)$$

where n is the electron density, B the large-scale magnetic field strength (by "large-scale," we mean the magnetic field on scales much larger than the electron Larmor radius and at frequencies much lower than the electron gyration frequency), and $T_{e,\parallel}$ and $T_{e,\perp}$ are the electron temperature parallel and perpendicular to the local magnetic field, respectively. The term $de_{w,e}$ on the right hand side of Equations (1) and (2) represents the total energy per particle transferred to waves, including magnetic, electric, and bulk kinetic contributions.[6]

Note that the CGL double adiabatic theory of Chew et al. (1956) predicts that, for adiabatic perturbations, $T_{e,\perp} \propto B$ and $T_{e,\parallel} \propto (n/B)^2$, which follow from the conservation of the first and second adiabatic invariants. The first square bracket on the right-hand side of Equations (1) and (2) explicitly shows that a mechanism to break the adiabatic invariance is needed for entropy production. In most cases, it is the temperature anisotropy (see the second square bracket on the right-hand side of Equations (1) and (2)) that provides the free energy for generating the waves responsible for breaking the adiabatic invariance.

2.1. Our Reference Shock

In Paper I, we validated the heating model summarized above by performing PIC simulations with the electromagnetic PIC code TRISTAN-MP (Buneman 1993; Spitkovsky 2005) for a representative shock with sonic Mach number $M_s = 3$ and plasma beta $\beta_{p0} = 16$. The Mach number

$$M_s = \frac{V_1}{c_s} = \frac{V_1}{\sqrt{2\Gamma k_{\rm B} T_0/m_i}} \quad (3)$$

[5] Our analysis applies equally to electrons and protons, even though below we focus only on electron entropy.

[6] If the equations above were to be applied to protons, the corresponding term should include not only the energy residing in proton-driven waves, but also the energy lost by performing work on the electron plasma (see Paper I).

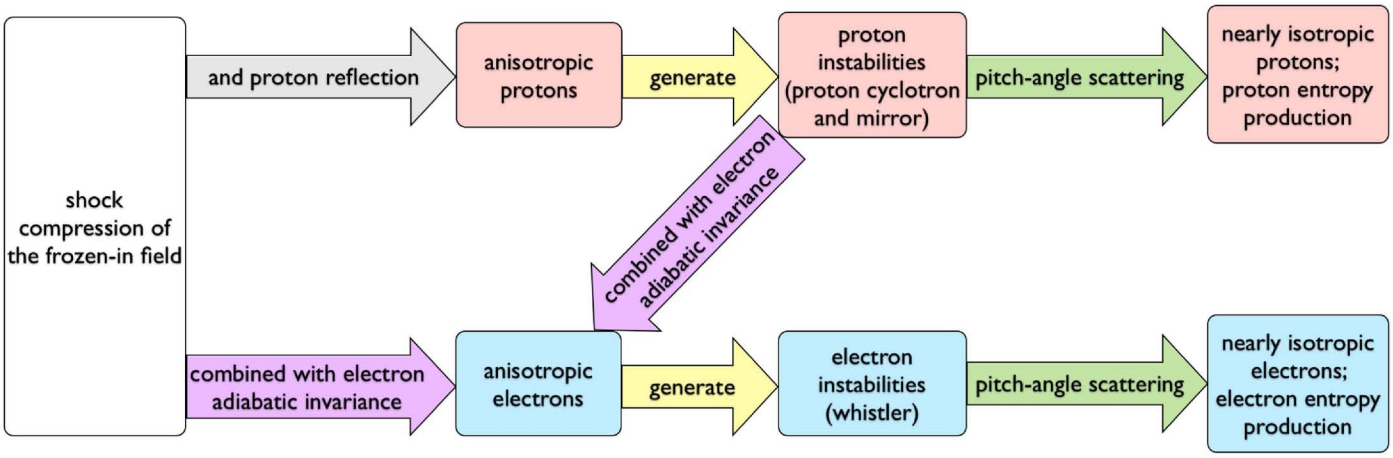

Figure 1. Schematic summary of the mechanism of irreversible heating of protons and electrons as described in Paper I.

is defined as the ratio between the upstream flow velocity V_1 in the shock frame and the upstream sound speed $c_s = \sqrt{2\Gamma k_B T_0/m_i}$. Here, T_0 is the upstream temperature (the same for both species, so $T_{e0} = T_{i0} = T_0$), k_B is the Boltzmann constant, $\Gamma = 5/3$ is the adiabatic index for an isotropic non-relativistic gas, and m_i is the proton mass. The upstream magnetic field strength is parameterized by the plasma beta

$$\beta_{p0} = \frac{8\pi n_0 k_B (T_{i0} + T_{e0})}{B_0^2} = \frac{16\pi n_0 k_B T_0}{B_0^2}, \quad (4)$$

where $n_{i0} = n_{e0} = n_0$ is the number density of the incoming protons and electrons. Alternatively, one could quantify the magnetic field strength via the Alfvénic Mach number $M_A = M_s\sqrt{\Gamma\beta_{p0}/2}$.

In Paper I, we considered a reference perpendicular shock with $M_s = 3$ and $\beta_{p0} = 16$ and showed that Equations (1) and (2) were in excellent agreement with the measured increase in electron entropy per particle (or specific entropy) across the shock, which can be computed directly from the electron distribution function $f_e(\boldsymbol{p})$ as

$$s_e \equiv -\frac{\int d^3p\, f_e \ln f_e}{\int d^3p\, f_e}. \quad (5)$$

In the reference shock, we found that efficient electron entropy production occurs at two major sites: at the shock ramp, where density compression coupled to flux freezing leads to field amplification (we call this scenario "case A"); and farther downstream, where long-wavelength magnetic waves (more specifically, proton cyclotron and mirror modes) accompanying the relaxation of the temperature anisotropy of post-shock protons can also contribute to magnetic field growth (we call this scenario "case B"). At both locations, field amplification coupled to adiabatic invariance drives the electrons to a large degree of temperature anisotropy, exceeding the threshold of the electron whistler instability. The resulting electron whistler waves—whose presence is one of the common denominators at the two sites mentioned above—cause efficient pitch angle scattering, which leads to violation of the electron adiabatic invariance and allows for entropy increase.

In Paper I, we studied cases A and B in detail by employing controlled periodic box experiments meant to reproduce the shock conditions at the two major sites of entropy production. In particular, the shock physics in the ramp (case A) can be replicated in a periodic box where the PIC equations are modified to allow for a continuous large-scale compression, as in Sironi & Narayan (2015), Sironi (2015). While we studied this scenario only for our reference case with $M_s = 3$ and $\beta_{p0} = 16$ in Paper I, we extensively explore a range of Mach numbers and plasma betas in Section 3 of the present paper. In Paper I, we also investigated the physics of electron heating via anisotropy-driven proton waves (case B) by means of a periodic box initialized with anisotropic protons, with a degree of anisotropy inspired by our reference case with $M_s = 3$ and $\beta_{p0} = 16$. In Section 4, we extend the same analysis to a wide range of flow conditions.

The advantage of the periodic domains is twofold: (i) they allow for more direct control of the relevant physics; and (ii) due to less demanding computational requirements, they permit our investigation to be extended up to the realistic mass ratio. In Paper I, we were able to ascertain that the electron entropy increase has only a weak dependence on mass ratio (less than a $\sim$30% drop, as we increase the mass ratio from $m_i/m_e = 49$ up to $m_i/m_e = 1600$).

3. Electron Heating by Shock Compression of the Upstream Field

In this section, we focus on case A, i.e., we investigate the efficiency of electron heating (and its dependence on the flow conditions) when the field amplification that induces the electron anisotropy—which in turn leads to electron whistler waves, and then to entropy increase—is due exclusively to the large-scale density compression occurring in the shock ramp.

3.1. Simulation Setup

The simulation setup parallels the one employed in Section 5 of Paper I, which we summarize here for completeness. We set up a suite of compressing box experiments, using the method introduced in Sironi & Narayan (2015) and Sironi (2015), which redefined the unit length of the axes such that a particle subject only to compression stays at fixed coordinates in the primed system. Next, compression with rate q is accounted for

by the diagonal matrix

$$\boldsymbol{L} = \frac{\partial \boldsymbol{x}}{\partial \boldsymbol{x}'} = \begin{pmatrix} (1+q\,t)^{-1} & 0 & 0 \\ 0 & 1 & 0 \\ 0 & 0 & 1 \end{pmatrix}, \tag{6}$$

which has been tailored for compression along the x axis, perpendicular to the uniform ordered magnetic field $\boldsymbol{B}_0$ initialized along the y direction (in analogy to the shock setup that we will discuss in Section 5). Maxwell's equations in the primed coordinate system automatically account for flux freezing (i.e., the field grows in time as $\boldsymbol{B}_0(1+q\,t)$, in the same way as the density $n = n_0(1+q\,t)$), and the form of the Lorentz force in the primed system guarantees the conservation of the first and second adiabatic invariants.

Becase we have shown, in Paper I, that the wavevector of the whistler mode is nearly aligned with the field direction (i.e., along $\hat{y}$), we employ 1D simulations with the computational box oriented along y. However, all three components of electromagnetic fields and particle velocities are tracked. In 1D simulations, we can employ a large number of particles per cell (we use 1600 particles per species per cell) so we have adequate statistics for the calculation of the electron specific entropy from the phase space distribution function, as in Equation (5).

As a result of the large-scale compression encoded in Equation (6), both electrons and protons will develop a temperature anisotropy, and we should witness the development of both electron and proton anisotropy-driven modes. However, as was the case in Paper I, our goal is to isolate the role of the large-scale field amplification (as expected in the shock ramp) in generating electron irreversible heating, regardless of the presence of proton-driven modes (which will be the focus of Section 4). For this reason, in our compressing box runs, we artificially inhibit the update of the proton momentum (this effectively corresponds to the case of infinitely massive protons). A similar strategy, but in the case of field amplification driven by shear rather than compression, has been employed by Riquelme et al. (2017).

The compression rate q (which we cast in units of $\Omega_{\rm ci} = eB_0/m_i c$, i.e., the proton Larmor frequency in the initial field B_0) is measured directly from our shock simulations described in Section 5. In fact, we can quantify the profile of electron density as a function of the co-moving time of the electron fluid

$$\tau \equiv \int \frac{dx'}{V_{\rm xe}(x')}, \tag{7}$$

where $V_{\rm xe}$ is the electron fluid velocity in the shock frame, and the integral goes from the upstream to the downstream region.[7] Figure 2 shows the electron density profile as a function of τ for a suite of shock simulations with $\beta_{p0} = 16$ and varying Mach number (solid lines, as indicated in the legend), which will be discussed in Section 5. The faster rise seen for higher values of M_s is driven by the fact that the density jump across the shock monotonically increases with Mach number, for two reasons. First, the density jump from upstream to downstream as derived from the Rankine–Hugoniot relations is a monotonically increasing function of M_s. Second, the density overshoot in the shock ramp also increases with M_s (Leroy 1983; see also Figure 7 in Section 5). Because the thickness of the shock is nearly independent of Mach number (and always on the order of the proton Larmor radius), a larger density jump for higher M_s corresponds, in Figure 2, to a faster compression rate. In fact, if we model the density compression as a linear function of time (dashed lines in Figure 2), the resulting compression rate q steadily increases with M_s. The values of q adopted in the periodic simulations discussed in this section are given in Table 1, in units of the proton Larmor frequency $\Omega_{\rm ci}$ (all the runs presented in this section employ a reduced mass ratio $m_i/m_e = 49$). We wish to emphasize that the value of the shock Mach number enters the compressing box experiments presented here only via the compression rate q (i.e., M_s should be meant as the Mach number of the shock simulation that corresponds to a given choice of q for the compressing box).

We summarize our physical and numerical parameters in Table 1 (the run names have the suffix "c" to indicate that we employ compressing boxes). The first four runs explore the dependence on Mach number (or equivalently, compression rate) for fixed $\beta_{p0} = 16$, whereas the last four simulations investigate the dependence on β_{p0} for a fixed compression rate $q = 2.5\,\Omega_{\rm ci}$, as appropriate for a shock with $M_s = 3$. In all the runs, we initialize a population of isotropic electrons with temperature $T_{e0} = 10^{-2} m_e c^2/k_{\rm B}$. We resolve the electron skin depth

$$\frac{c}{\omega_{\rm pe}} = \sqrt{\frac{m_e c^2}{4\pi e^2 n_0}} \tag{8}$$

with 10 cells, so the Debye length is marginally resolved. The box extent along the y direction is fixed at $86\,c/\omega_{\rm pe}$ for $\beta_{p0} \leqslant 16$, which is sufficient to capture several wavelengths of the electron whistler instability. For $\beta_{p0} = 32$ and 64, we increase the box length roughly as $\propto\sqrt{\beta_{p0}}$, because the wavelength of whistler waves increases with plasma beta (see Appendix B, where we study the linear dispersion properties of the whistler instability).

3.2. Dependence on M_s

Figure 3 compares the results of compressing box simulations (runs `Ms2c`, `Ms3c`, `Ms4c`, and `Ms5c` in Table 1) with the same $\beta_{p0} = 16$ and different compression rates q (or equivalently, different Mach numbers of the corresponding shock simulations). We present the evolution of the whistler wave energy (panel (a)), the electron temperature anisotropy (panel (b)), the rate $-d\ln(T_{e,\perp}/B)$ of breaking adiabatic invariance (panel (c)), and the electron entropy increase (panel (d)) when varying the compression rate from $q/\Omega_{\rm ci} = 1.5$ up to 4.0 (from blue to red, see the legend in the first panel). For mass ratio $m_i/m_e = 49$, the compression rate in units of the electron gyration frequency $\Omega_{\rm ce} = (m_i/m_e)\Omega_{\rm ci}$ is $q/\Omega_{\rm ce} \simeq 0.02(q/\Omega_{\rm ci}) \ll 1$, i.e., compression occurs slowly as compared to the electron gyration time (so our choice of $m_i/m_e = 49$ fulfills the requirement $q/\Omega_{\rm ce} \ll 1$ expected for the realistic mass ratio).

As a result of the large-scale compression, the electron perpendicular and parallel temperatures are expected to scale as $T_{e,\perp} \propto B \propto (1+qt)$ and $T_{e,\parallel} \propto (n/B)^2 \propto$ const, according to

[7] As described in Section 5, the shock propagates along $+\hat{x}$ in our simulations.

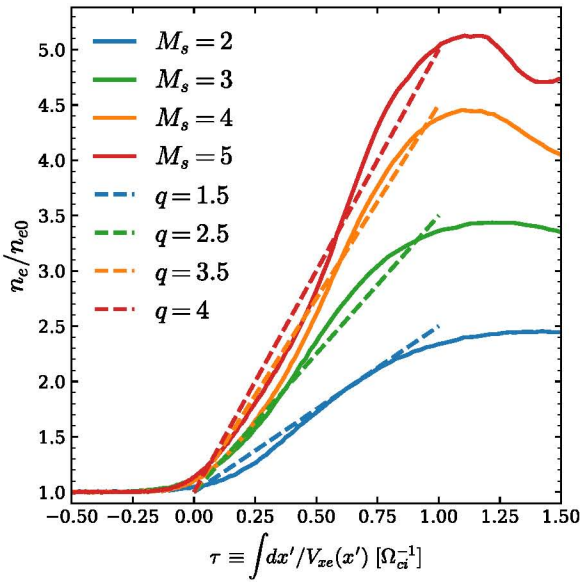

Figure 2. Density compression experienced by electrons (solid lines) as they propagate from upstream to downstream, as a function of the electron comoving time, from our suite of shock simulations (see Section 5) with fixed $\beta_{p0} = 16$ and varying M_s (as indicated in the legend). Dotted lines show the linear approximation $n_e/n_{e0} = (1 + qt)$ (with values of q indicated in the legend) employed in the compressing box experiments.

Table 1
Parameters for the Compressing Box Experiments Described in Section 3

run name	M_s	q	β_{p0}	$k_B T_{e0}/m_e c^2$	L_y $[c/\omega_{pe}]$
Ms2c	2	1.5	16	10^{-2}	86
Ms3c/beta16c	3	2.5	16	10^{-2}	86
Ms4c	4	3.5	16	10^{-2}	86
Ms5c	5	4	16	10^{-2}	86
beta4c	3	2.5	4	10^{-2}	86
beta8c	3	2.5	8	10^{-2}	86
beta32c	3	2.5	32	10^{-2}	130
beta64c	3	2.5	64	10^{-2}	173

Note. The compression rate q is in units of the proton larmor frequency Ω_{ci}, for mass ratio $m_i/m_e = 49$.

the double adiabatic theory. In fact, the electron anisotropy at early times grows as $T_{e,\perp}/T_{e,\parallel} - 1 = qt$ (Figure 3(b)), and thus, at a faster rate for higher q (or equivalently, in higher M_s shocks).

The increasing temperature anisotropy leads to the exponential growth of the electron whistler instability. When the energy in whistler waves reaches a fraction $\sim 10^{-2}$ of the compressed background field energy (Figure 3(a)), the waves are sufficiently strong to scatter the electrons in pitch angle, breaking their adiabatic invariance and decreasing the electron anisotropy. In fact, the peak in panel (c), i.e., the time when the electron adiabatic invariance is most violently broken, always corresponds to the time when the electron anisotropy in panel (b) shows the sharpest decrease. This occurs earlier for higher q (if time is measured in Ω_{ci}^{-1}, as in Figure 3), because electrons are driven sooner to large levels of anisotropy. As a result of efficient pitch angle scattering, the electron anisotropy is reduced to the marginal stability threshold of the electron

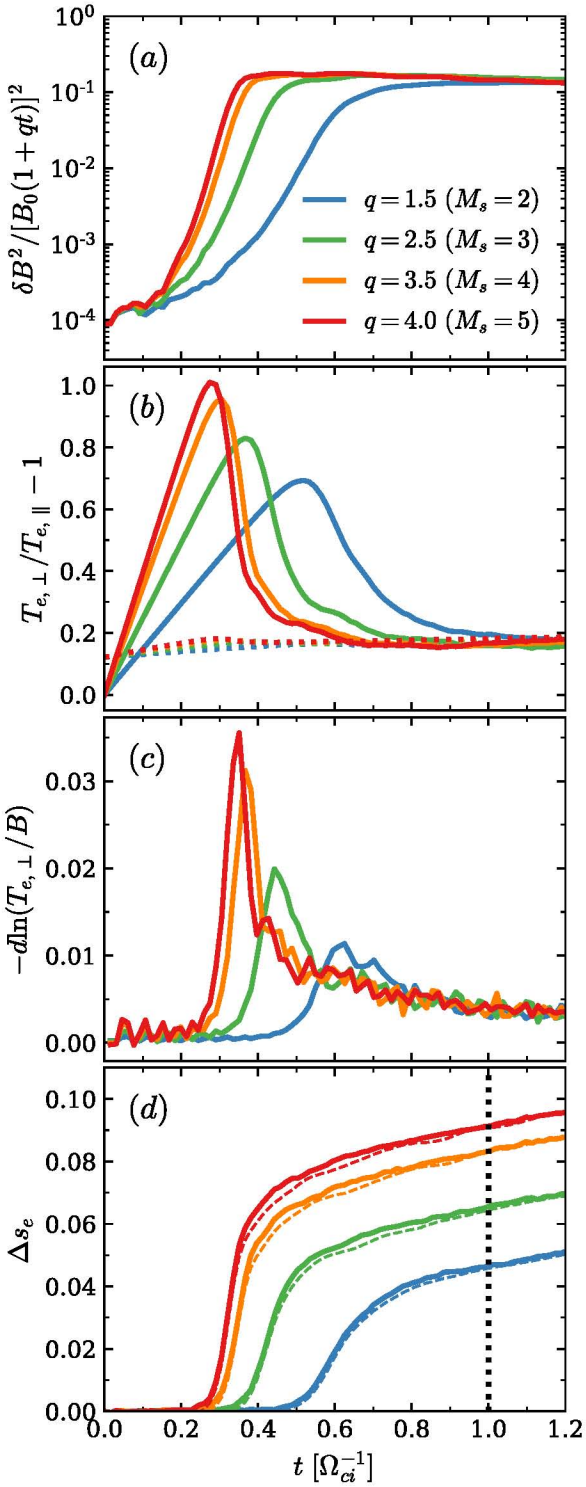

Figure 3. Dependence on M_s, or equivalently compression rate q, of various space-averaged quantities in compressing box experiments Ms2c, Ms3c, Ms4c, and Ms5c, at fixed β_{p0}. As a function of time in units of Ω_{ci}^{-1}, we plot: (a) energy in magnetic field fluctuations, normalized to the energy of the compressed field; (b) electron temperature anisotropy (solid lines) and threshold condition for the electron whistler instability (dotted lines with the same color coding as the solid lines); (c) rate of violation of adiabatic invariance $-d\ln(T_{e,\perp}/B)$; (d) electron entropy change, measured from the electron distribution function as in Equation (5) (solid lines) and predicted from our heating model of Equation (1) (thin dashed lines). The vertical dotted black line in panel (d) marks the approximate end of the compression phase in the shock ramp.

whistler instability (Gary 2005)

$$\frac{T_{e,\perp}}{T_{e,\parallel}} - 1 \simeq \frac{0.21}{\beta_{e,\parallel}^{0.6}} \quad (9)$$

(dotted lines in Figure 3(b), with the same color coding as in the legend of panel (a)), which is nearly the same for all the runs, as they start with the same β_{p0} and maintain a similar value of $\beta_{e,\parallel}$. Here, $\beta_{e,\parallel}$ is the electron plasma beta measured with the parallel temperature $T_{e,\parallel}$.

Near the end of the exponential growth of whistler waves, the electron entropy shows a rapid increase (panel (d)). Here, the electron anisotropy is still large, and at the same time, whistler waves are sufficiently powerful to provide effective pitch-angle scattering. In other words, both terms in the square brackets of either Equation (1) or (2) are large. The resulting entropy increase is a monotonic function of q, for the following reason. First, larger values of q allow the electrons to reach higher levels of peak anisotropy (Figure 3(b)). This can be understood from the competition between the large-scale compression rate (which increases the electron anisotropy) and the growth rate of whistler waves (which try to reduce the anisotropy via pitch angle scattering). Because the whistler growth rate depends on how much the anisotropy exceeds the whistler threshold in Equation (9), a higher anisotropy is needed for larger q (in fact, Figure 3 shows that the whistler growth rate is higher for larger q). Second, because whistler waves are sourced by the free energy in electron anistropy, the wave energy at saturation will be larger for higher q (Figure 3(a)). Third, stronger whistler waves will be more efficient in breaking the electron adiabatic invariance (Figure 3(c)). The combination of these effects explains the monotonic trend in electron entropy observed in Figure 3(d) near the end of the exponential growth of whistler waves (i.e., at the time of sharp increase in the curves of panel (d)).

After the exponential growth, electron whistler waves enter a secular phase where the wave energy (normalized to the compressed background field energy) stays almost constant in time. At this point, the whistler wave energy is also nearly independent of q (panel (a)), and the same will hold for the rate of violation of electron adiabatic invariance (panel (c)). The electron anisotropy settles around the threshold of marginal stability (compare the solid and dotted lines in panel (b) at late times), which is independent of q at fixed $\beta_{e,\parallel}$. It follows that the rate of increase of electron entropy during the secular phase will be the same regardless of q, as is confirmed by panel (d) (see slow growth at late times, at a rate independent of q). We remark that the overall increase of electron entropy, as measured directly from our simulations using Equation (5), is in excellent agreement with our heating model of Equation (1) (compare solid and thin dashed lines in panel (d), respectively).

From Figure 3(d), we can infer how the entropy increase in the shock ramp should scale with Mach number, if field amplification is induced by shock-compression of the upstream field (case A). Because the compression in the shock ramp lasts about one proton gyration time, we compare the entropy curves at $\Omega_{ci}t \sim 1$, as indicated by the vertical dotted black line in panel (d). We then find that the efficiency of electron heating in the shock ramp is expected to be larger at higher M_s (corresponding to faster compressions in Figure 3), at fixed β_{p0}. We will confirm this trend in our shock simulations presented in Section 5. However, we anticipate that, in shocks with high Mach number, proton-driven waves already appear near the shock ramp. In this case, large-scale field compression and proton-driven waves (as discussed in Section 4) co-exist and co-contribute to efficient electron entropy production in the shock transition region.

3.3. Dependence on β_{p0}

In this subsection, we study the dependence of the electron heating efficiency on plasma beta β_{p0}, by means of compressing box experiments (as appropriate for case A). We fix the compression rate at $q = 2.5\,\Omega_{ci}$, as appropriate for a shock with $M_s = 3$, and vary the initial plasma beta β_{p0} from 4 to 64 (runs `beta4c`, `beta8c`, `beta16c`, `beta32c`, `beta64c`).

Figure 4 compares the results of our runs. Initially, the electron temperature anisotropy increases as $T_{e,\perp}/T_{\parallel} - 1 = qt$, regardless of β_{p0} (panel (b)). Eventually, this leads to the development of the whistler instability, whose exponential growth needs to balance the large-scale compression (so its growth rate is nearly independent of β_{p0}, as confirmed by panel (a)). As we discuss in Appendix B, a given growth rate of the whistler mode requires a lower degree of electron anisotropy for higher plasma beta, which explains the trend in peak anisotropy of Figure 4(b). In turn, a lower level of peak anisotropy corresponds to a smaller amount of free energy available to be converted into whistler waves, whose amplitude is indeed weaker at higher β_{p0} (see the inset in Figure 4(a), where we normalize the whistler wave pressure with respect to the electron parallel pressure $nk_{B}T_{e,\parallel}$). Weaker whistler wave activity at higher β_{p0} explains why the breaking of electron adiabatic invariance is less violent at higher beta (panel (c)). Because both the electron anisotropy and the violation of adiabatic invariance are weaker for larger β_{p0}, the resulting entropy increase near the end of the exponential phase of whistler growth is smaller for a higher plasma beta, as shown in Figure 4(d) (solid lines; compare the values attained during the early phase of rapid growth).

In the secular phase of the electron whistler instability, when efficient pitch angle scattering has brought the anisotropy down to the threshold of marginal stability (dotted lines in Figure 4(b), with the same color coding as the solid lines), the electron entropy keeps increasing, yet at a slower rate. In the secular phase, the trend discussed above still holds (i.e., weaker entropy production at higher plasma beta), primarily because the degree of electron anisotropy stays smaller at higher β_{p0} (panel (b)), due to the monotonic dependence on $\beta_{e,\parallel}$ of the threshold of marginal stability; see Equation (9). As we have emphasized in the previous subsection, the increase of electron entropy in both exponential and secular phases, as measured directly from our simulations (Equation (5)), is in excellent agreement with our heating model of Equation (1) (compare solid and thin dashed lines in panel (d), respectively).

In summary, when field amplification is due to compression alone (case A), the efficiency of electron entropy production decreases monotonically with increasing plasma beta. In particular, this holds after one proton gyration time (see the vertical dotted black line in panel (d)), which we have taken to be the characteristic compression time in the shock ramp. However, as we shall see in the next section, the dependence on β_{p0} is opposite when field amplification is provided by proton-driven waves. As a result of the two opposite trends, in our shock simulations of Section 5, where both compression and proton-driven waves contribute to field amplification, the dependence on β_{p0} is rather weak in the range of plasma beta that we explore.

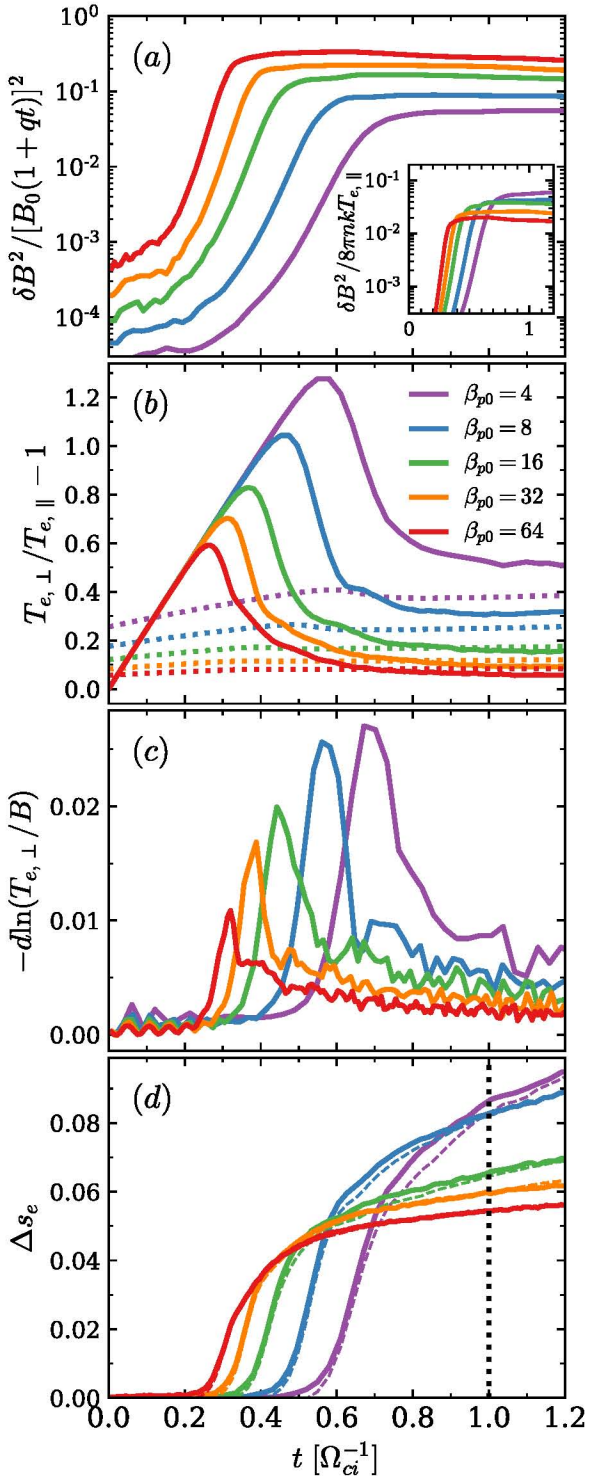

Figure 4. Dependence on β_{p0} of various space-averaged quantities in compressing box experiments `beta4c`, `beta8c`, `beta16c`, `beta32c`, and `beta64c`, at fixed $M_s = 3$. As a function of time in units of Ω_{ci}^{-1}, we plot: (a) energy in magnetic field fluctuations, normalized to the energy of the compressed field—in the inset, we also plot the pressure in magnetic field fluctuations normalized by the electron parallel pressure; (b) electron temperature anisotropy (solid lines) and threshold condition for the electron whistler instability (dotted lines with the same color coding as the solid lines); (c) rate of violation of adiabatic invariance $-d\ln(T_{e,\perp}/B)$; (d) electron entropy change, measured from the electron distribution function as in Equation (5) (solid lines) and predicted from our heating model of Equation (1) (thin dashed lines). The vertical dotted black line in panel (d) marks the approximate end of the compression phase in the shock ramp.

4. Electron Heating by Proton-driven Waves

In this section, we focus on case B, i.e., we investigate the efficiency of electron irreversible heating (and its dependence on the flow conditions) when field amplification is due exclusively to proton-scale waves induced by the relaxation of proton temperature anisotropy. To study this effect, we employ periodic boxes (not compressing, so with $q = 0$), where the degree of proton anisotropy is prescribed to mimic the conditions expected in the shock downstream. Because both the proton cyclotron instability, which dominates over the mirror mode in our runs (see Section 5), and the electron whistler instability have the fastest growing wavevector aligned with the background field, we employ 1D simulation domains aligned with the y-direction of the field.

4.1. Simulation Setup

We now describe how the initial conditions of our 1D periodic box experiments are set up to be representative of the downstream region of a shock with Mach number M_s and plasma beta β_{p0}. We need to prescribe the initial proton temperatures perpendicular and parallel to the magnetic field ($T_{i0\mathrm{box},\perp}$ and $T_{i0\mathrm{box},\parallel}$), the initial electron temperature ($T_{e0\mathrm{box}}$; as we justify below, we consider isotropic electrons), and the initial electron plasma beta ($\beta_{e0\mathrm{box}}$). We employ the subscript "box" to distinguish them from the initial conditions of our shock simulations. In principle, these parameters can be set by measuring directly the flow conditions behind our simulated shocks. However, we show below that they can be simply prescribed using the Rankine–Hugoniot jump conditions. This has the advantage of showing explicitly the expected dependence on the shock Mach number M_s and plasma beta β_{p0}.

Because the pre-shock flow moves along the x-direction, while the pre-shock magnetic field is oriented along y (see Section 5), the post-shock protons will be promptly gyrotropic in the plane xz perpendicular to the pre-shock field, but generally anisotropic with respect to the y-direction parallel to the field. In the absence of instabilities that mediate efficient isotropization, the motions perpendicular and parallel to the field are effectively decoupled, and the post-shock protons behave as a plasma with two degrees of freedom (ergo, with adiabatic index $\Gamma = 2$). This is demonstrated by the 2D out-of-plane and 1D shock simulations shown in Appendix A of Paper I. The density and temperature jumps across a shock with adiabatic index $\Gamma = 2$ (as appropriate for the region just behind the shock) are

$$r_{\mathrm{RH},\Gamma=2} = \frac{3\beta_{p0}M_s^2}{2+\beta_{p0}(2+M_s^2)}, \tag{10}$$

$$\Delta t_{\mathrm{RH},\Gamma=2} = M_s^2\left(2-\frac{2}{r_{\mathrm{RH},\Gamma=2}^2}\right)+\frac{4-4\,r_{\mathrm{RH},\Gamma=2}}{\beta_{p0}}+4, \tag{11}$$

where $\Delta t_{\mathrm{RH},\Gamma=2}$ is, more precisely, the jump in the perpendicular temperature for the overall fluid (the parallel one stays unchanged).

We then assume that the electron temperature jump in the perpendicular direction follows from the adiabatic law (in Section 5, we quantify the efficiency of electron irreversible heating; still, for the parameter regime we explore, most of the electron temperature increase comes from adiabatic

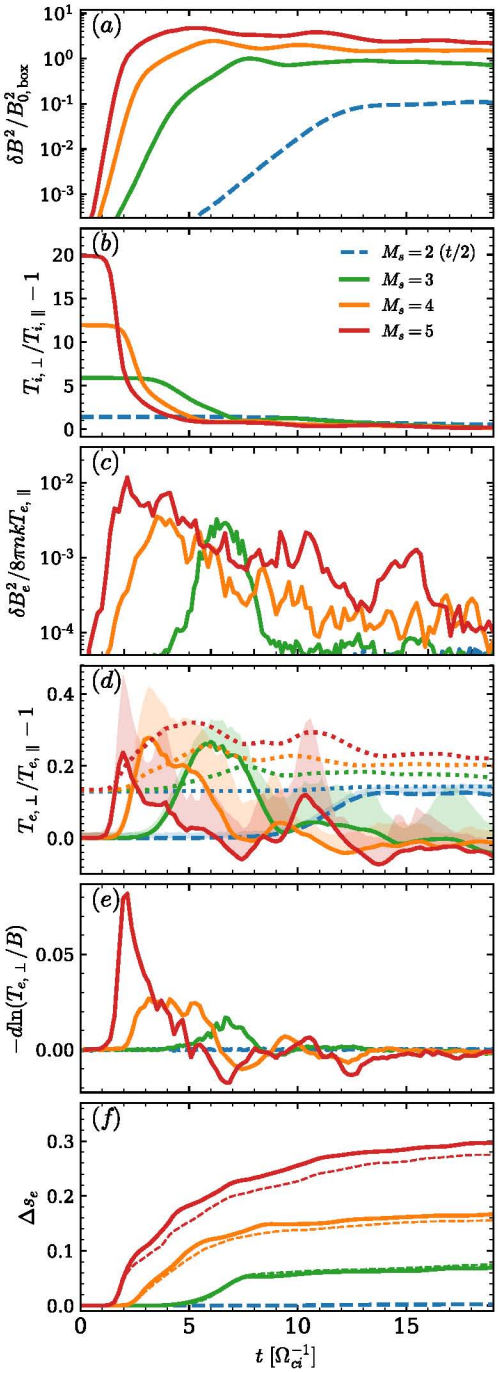

Figure 5. Dependence on M_s of various quantities in periodic box experiments with anisotropic protons (runs `Ms2nc`, `Ms3nc`, `Ms4nc`, `Ms5nc`), at fixed $\beta_{p0} = 16$. As a function of time in units of Ω_{ci}^{-1}, we plot: (a) energy in magnetic field fluctuations, normalized to the energy of the initial field in the box $B_{0,\rm box}$; (b) proton temperature anisotropy; (c) magnetic pressure in electron-scale fluctuations, normalized to the electron parallel pressure; (d) electron temperature anisotropy (solid lines for the box-averaged values, shaded regions for the 50–90 percentiles) and threshold of the electron whistler instability (dotted lines with the same color coding as the solid lines); (e) rate of violation of the electron adiabatic invariance $-d\ln(T_{e,\perp}/B)$; (f) electron entropy change, measured from the electron distribution function as in Equation (5) (solid lines) and predicted from our heating model of Equation (1) (thin dashed lines). The time axis of the $M_s = 2$ run (blue dashed lines) is reduced by a factor of two for better comparison. To isolate whistler-like waves in panel (c), we have applied a high-pass filter that retains frequencies higher than $0.064\ \Omega_{ce}$ and wavelengths shorter than $25\ c/\omega_{pe}$.

compression). Coupling electron adiabatic invariance with flux freezing, this implies that the post-shock electron temperature is $r_{\rm RH,\Gamma=2}\ T_0$. From Equation (11), which prescribes the jump in perpendicular temperature for the overall (electron + proton) fluid, we find that the post-shock proton temperature in the direction perpendicular to the field, which we take as the initial condition $T_{i0\rm box,\perp}$ in our periodic boxes, will be

$$T_{i0\rm box,\perp} = T_0(2\ \Delta t_{\rm RH,\Gamma=2} - r_{\rm RH,\Gamma=2}). \tag{12}$$

The parallel proton and electron temperatures are the same as in the pre-shock region; in particular,

$$T_{i0\rm box,\parallel} = T_0. \tag{13}$$

With regard to the initialization of electrons, we assume that the electron anisotropy is rapidly erased due to the rapid development of electron-scale instabilities, as it indeed occurs in the shock ramp.[8] If this happens without any energy exchange with the protons, the isotropic electron temperature is

$$T_{e0\rm box} = T_0\frac{2\ r_{\rm RH,\Gamma=2} + 1}{3}. \tag{14}$$

Finally, the initial electron plasma beta can be computed from flux freezing as

$$\beta_{e0\rm box} = \frac{2\ r_{\rm RH,\Gamma=2} + 1}{3\ r_{\rm RH,\Gamma=2}}\frac{\beta_{p0}}{2}. \tag{15}$$

The physical and numerical parameters used for the periodic box experiments of this section are summarized in Table 2 (the run names have the suffix "nc" to indicate that the boxes are not compressing). We indicate the Mach number M_s and plasma beta β_{p0} of the corresponding shock simulations, the initialization values of $k_{\rm B}T_{i0\rm box,\parallel}/m_i c^2$, $T_{i0\rm box,\perp}/T_{i0\rm box,\parallel}$, $T_{e0\rm box}/T_{i0\rm box,\parallel}$, and $\beta_{e0\rm box}$ employed in the periodic boxes, the number of computational particles per cell ($N_{\rm ppc}$), and the box length L_y along the y-direction of the background large-scale field, in units of the proton skin depth $c/\omega_{\rm pi} = \sqrt{m_i/m_e}\ c/\omega_{\rm pe}$. We employ a reduced mass ratio $m_i/m_e = 49$. From Table 2, it is apparent that the Mach number M_s has a pronounced effect on the initial proton anisotropy. In fact, in the limit of $M_s \gg 1$, we have $r_{\rm RH,\Gamma=2} \propto M_s^0$ and $\Delta t_{\rm RH,\Gamma=2} \propto M_s^2$, so that $T_{i0\rm box,\perp}/T_{i0\rm box,\parallel} \propto M_s^2$ from Equations (12) and (13).

4.2. Dependence on M_s

In this subsection, we compare the periodic box simulations `Ms2nc`, `Ms3nc`, `Ms4nc`, `Ms5nc`, that correspond to shocks with fixed $\beta_{p0} = 16$ but different M_s, ranging from 2 to 5. Our results are shown in Figure 5. The case corresponding to $M_s = 2$ is plotted with a dashed line to emphasize that its time axis has been reduced by a factor of two, to facilitate comparison with the other cases.

As we have discussed above (see also Table 2), runs with larger M_s are initialized with a stronger degree of proton anisotropy (see the curves in panel (b) at the initial time). In response to the greater amount of free energy stored in proton temperature anisotropy, runs with larger M_s develop stronger proton cyclotron waves (panel (a)). In addition, because the growth rate of the proton cyclotron instability is higher for larger temperature anisotropies, at fixed plasma beta (see the linear dispersion properties of the proton cyclotron instability in Appendix C), the proton cyclotron wave energy grows faster

[8] Despite the fact that we now assume isotropic electrons, the ansatz of a $\Gamma = 2$ gas that we employed to calculate the jump conditions will still hold because the post-shock pressure is mostly contributed by protons (see Section 5).

Table 2
Parameters for the Anisotropic Protons Box Experiments Described in Section 4

Run Name	M_s	β_{p0}	$k_B T_{i0\mathrm{box},\parallel}/m_i c^2$	$T_{i0\mathrm{box},\perp}/T_{i0\mathrm{box},\parallel}$	$T_{e0\mathrm{box}}/T_{i0\mathrm{box},\parallel}$	$\beta_{e0\mathrm{box}}$	N_{ppc}	L_y $[c/\omega_{\mathrm{pi}}]$
Ms2nc	2	16	2×10^{-4}	2.88	1.64	6.69	10^4	30.9
Ms3nc/beta16nc	3	16	2×10^{-4}	6.87	1.95	6.43	10^4	30.9
Ms4nc	4	16	2×10^{-4}	12.86	2.10	6.34	10^4	30.9
Ms5nc	5	16	2×10^{-4}	20.74	2.18	6.30	10^4	30.9
beta8nc	3	8	2×10^{-4}	6.69	1.93	3.22	10^4	30.9
beta32nc	3	32	2×10^{-4}	6.96	1.96	12.85	10^4	30.9
beta64nc	3	64	2×10^{-4}	7.00	1.96	25.69	2×10^4	46.3

Note. We employ a fixed mass ratio $m_i/m_e = 49$ and resolve the electron skin depth with seven cells, which is sufficient to capture the electron debye length.

at higher M_s (panel (a)). Because pitch angle scattering by the proton cyclotron modes is responsible for relaxing the temperature anisotropy, this explains why the proton anisotropy in Figure 5(b) drops faster for higher M_s, despite starting from higher initial values.

The growth of proton cyclotron waves provides a source of field amplification that can perform work on the electrons. However, this does not automatically lead to irreversible electron heating. In fact, Figure 5 shows that, for $M_s = 2$ the energy in proton cyclotron modes is so small (dashed blue line in panel (a)) that the electron temperature anisotropy (dashed blue line in panel (d)) never exceeds the threshold of the electron whistler instability (indicated in Figure 5(d) by the corresponding dotted blue line). In fact, in this case, no whistler waves are observed to grow (no blue line appears in Figure 5(c), where we plot the magnetic pressure associated with whistler waves in units of the electron parallel pressure). In the absence of whistler waves, the electron evolution stays adiabatic (dashed blue line in panel (e)), and no electron entropy is generated (dashed blue line in panel (f)).

For higher M_s, the proton waves are sufficiently strong to drive the electron anisotropy beyond the whistler threshold (compare solid and dotted lines of the same color in Figure 5(d)). Because whistler waves provide the pitch-angle scattering required to break adiabatic invariance, this leads to electron entropy production (Figure 5(f)). As shown in Figure 5(f), the increase in electron entropy is a monotonic function of M_s. As we now discuss, this is related to the fact that the same trend holds separately for the two terms in square brackets of Equation (1) (or equivalently, Equation (2)).

In fact, the degree of violation of electron adiabatic invariance is larger for higher M_s (Figure 5(e)), because whistler waves are more powerful (Figure 5(c)).[9] The trend in electron anisotropy (Figure 5(d)) is less clear, with the green, orange, and red curves showing comparable peak values. Unlike in the compressing box experiments of the previous section, where the degree of electron anisotropy was roughly uniform throughout the simulation domain, here proton-driven modes introduce large spatial variations in the electron properties (in analogy to Figure 11 of Paper I). It is then useful to complement the information on the box-averaged anisotropy (solid lines in Figure 5(d)) with shaded regions indicating the 50–90 percentiles of electron temperature anisotropy. This reveals that spatial variations in electron anisotropy are stronger at higher M_s (or equivalently, the distance between the solid curve and the upper boundary of the corresponding shaded region increases with M_s), where proton modes are also more powerful. In addition, runs with larger M_s present localized regions with systematically higher peak anisotropies (the peak of the shaded red region is higher than the orange one, which in turn is higher than the green one). On the one hand, this justifies the fact that the strength of whistler waves, which are seeded by electron anisotropy, increases with M_s. On the other hand, when coupled with the dependence on M_s of the violation of adiabatic invariance (Figure 5(e)), it fully justifies why runs with higher M_s lead to more efficient electron entropy production.

For low M_s, most of the entropy increase occurs near the end of the exponential phase of the proton cyclotron instability; by contrast, at high M_s, a steady growth in electron entropy is observed during the secular stage. Here, the strong cyclotron modes can occasionally excite local patches of electron anisotropy that exceed the whistler threshold (e.g., see the peak in the red shaded region at $\Omega_{\mathrm{ci}} t \sim 10.5$ in Figure 5(d)). The resulting whistler activity (see the corresponding peaks in the curves of panels (c) and (e)) can further increase the electron entropy.

Finally, we point out that, as we have also discussed in the case of compressing box simulations, the increase of electron entropy, as measured directly from our simulations (Equation (5)), is in excellent agreement with our heating model of Equation (1) (compare solid and thin dashed lines in panel (f), respectively).

4.3. Dependence on β_{p0}

In this subsection, we compare the periodic box simulations beta8nc, beta16nc, beta32nc, beta64nc, that correspond to shocks with fixed $M_s = 3$ but different β_{p0} ranging from 8 to 64. Our results are shown in Figure 6.

At fixed M_s, the initial proton temperature anisotropy is nearly independent of β_{p0} (see Figure 6(b) at early times). From the dispersion properties of the proton cyclotron mode (see Appendix C), the growth at fixed proton anisotropy is faster at higher plasma beta, in agreement with the exponential phase in Figure 6(a) and with the drop in proton anisotropy in Figure 6(b). At fixed proton anisotropy, the free energy available to be converted into proton waves will be larger with increasing β_{p0}, just because the proton thermal content is higher. In fact, when normalized to the magnetic energy of the large-scale field $B_{0,\mathrm{box}}$, the magnetic energy of proton cyclotron waves at saturation is larger for higher plasma beta, as shown in Figure 6(a).

In all the cases that we investigate, the growth of proton cyclotron waves drives the electron anisotropy above the whistler threshold (Figure 6(d), compare solid and dotted

[9] In order to obtain the magnetic energy $\delta B_e^2/8\pi$ in whistler-like fluctuations, we have applied a high-pass filter in frequency and wavenumber, as described in Paper I.

lines). At higher β_{p0}, the electron whistler instability starts earlier (Figure 6(c)), due to the combination of two effects: the proton waves grow faster, and the whistler threshold is lower, and thus easier to exceed.

In addition, the stronger proton waves generated for higher β_{p0} will have the chance to perform more work on the electrons. In particular, at higher β_{p0}, we expect that electrons will be driven further into the unstable region of the electron whistler mode (i.e., beyond the marginal stability threshold, which is itself a function of plasma beta, see Equation (9)). This is suggested by the general trend seen in Figure 6(d), where, e.g., the orange solid curve (for $\beta_{p0} = 32$) lies at $\Omega_{ci}t \sim 5$, significantly above the corresponding marginal stability threshold (indicated by the dotted orange line), whereas the solid blue line (for $\beta_{p0} = 8$) at $\Omega_{ci}t \sim 11$ is only marginally above the corresponding threshold (dotted blue curve). In turn, a higher level of electron anisotropy (with respect to the baseline provided by the marginal stability threshold) results in stronger whistler wave activity (Figure 6(c)), and in more violent breaking of electron adiabatic invariance (Figure 6(e)). It follows that the electron entropy increase will be more pronounced for higher β_{p0}, as confirmed by Figure 6(f).

We conclude this section with two comments. First, once again, our heating model is in good agreement with the measured entropy increase (compare thin dashed and solid lines in Figure 6(f)). Second, in the compressing box experiments of the previous section (meant to mimic field amplification by shock compression of the upstream field), higher values of plasma beta resulted in a weaker increase in electron entropy, but the opposite trend is observed here, where field amplification is due to proton cyclotron waves. In the shock simulations presented in the next section, where the two processes will co-exist, we should expect a weak dependence on plasma beta, as indeed we will find for the parameter regime we explore.

5. Electron Heating in Shocks

In the previous two sections, we have investigated the efficiency of electron irreversible heating when the magnetic field amplification that induces electron anisotropy—which in turn sources the growth of whistler waves and eventually results in entropy production—is due to two separate mechanisms: in Section 3, we have discussed case A, where field amplification is due to a large-scale density compression; in Section 4, we have focused on case B, where proton waves accompanying the relaxation of proton anisotropy can increase the magnetic field strength. In shocks, the two mechanisms co-exist, as we have already discussed in Paper I for our reference case with $M_s = 3$ and $\beta_{p0} = 16$. We now explore the dependence of irreversible electron heating in perpendicular shocks on Mach number and plasma beta. In Section 6, we summarize the key findings from the shock simulations and provide an empirical fit to our results, which can be used in comparison with the observations.

5.1. Simulation Setup

We perform shock simulations using the 3D electromagnetic PIC code TRISTAN-MP (Buneman 1993; Spitkovsky 2005). Our setup parallels closely what we have employed in Paper I. We use a 2D simulation box in the x–y plane, with periodic boundary conditions in the y-direction, but all three components of particle velocities and electromagnetic fields are

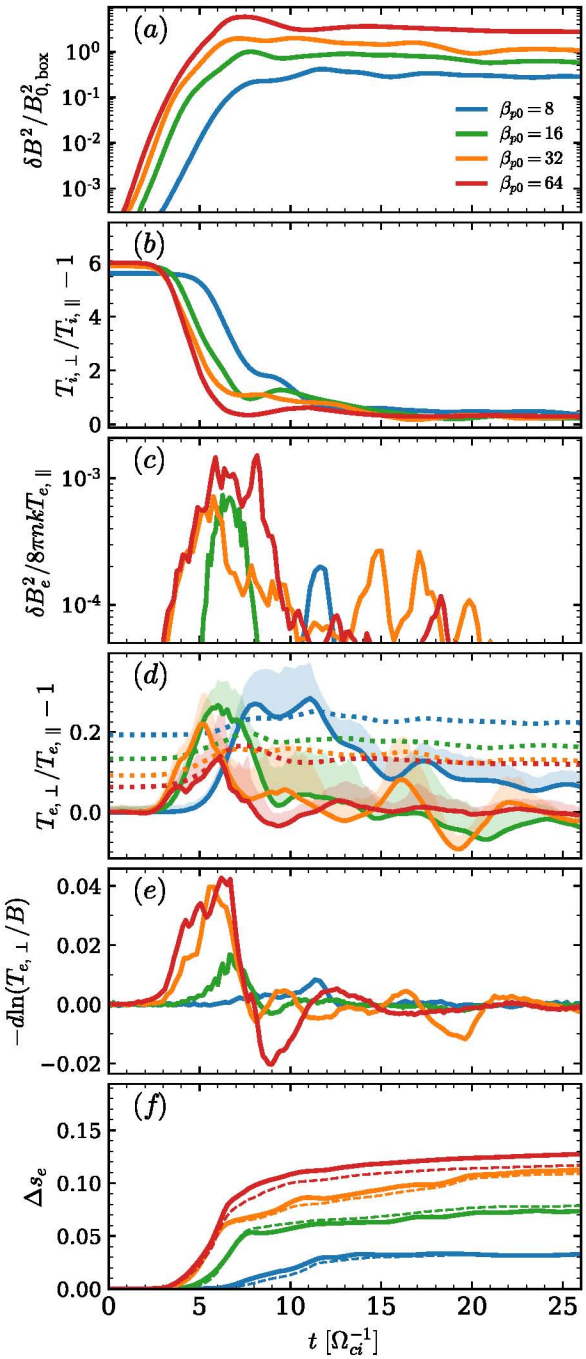

Figure 6. Dependence on β_{p0} of various quantities in periodic box experiments with anisotropic protons (runs `beta8nc`, `beta16nc`, `beta32nc`, `beta64nc`), at fixed $M_s = 3$. As a function of time in units of Ω_{ci}^{-1}, we plot: (a) energy in magnetic field fluctuations, normalized to the energy of the initial field in the box $B_{0,\rm box}$; (b) proton temperature anisotropy; (c) magnetic pressure in electron-scale fluctuations, normalized to the electron parallel pressure; (d) electron temperature anisotropy (solid lines for the box-averaged values, shaded regions for the 50–90 percentiles) and threshold of the electron whistler instability (dotted lines with the same color coding as the solid lines); (e) rate of violation of the electron adiabatic invariance $-d\ln(T_{e,\perp}/B)$; (f) electron entropy change, measured from the electron distribution function as in Equation (5) (solid lines) and predicted from our heating model of Equation (1) (thin dashed lines). To isolate whistler-like waves in panel (c), we have applied a high-pass filter: for run `beta8nc` (respectively, `beta16nc`, `beta32nc`, `beta64nc`) we retain frequencies higher than 0.063 Ω_{ce} (respectively, 0.063, 0.039, 0.039), and wavelengths shorter than 20 c/ω_{pe} (respectively, 25, 35, 35). These choices are motivated by the fact that the fastest growing mode of the electron whistler instability has lower frequencies and longer wavelengths for higher plasma beta.

Table 3
Parameters for the Shock Simulations Presented in Section 5

Run Name	M_s	$M_{s,\mathrm{meas}}$	β_{p0}	m_i/m_e	N_{ppc}	L_y $[c/\omega_{\mathrm{pi}}]$
Ms2beta4	2	2.13	4	49	32	21.6
Ms2beta8	2	2.11	8	49	32	21.6
Ms2beta16	2	2.16	16	49	32	21.6
Ms2beta32	2	2.11	32	49	32	21.6
Ms3beta4	3	3.04	4	49	32	21.6
Ms3beta8	3	3.03	8	49	32	21.6
Ms3beta16	3	2.98	16	49	32	21.6
Ms3beta32	3	2.95	32	49	32	21.6
Ms4beta4	4	4.06	4	49	32	21.6
Ms4beta8	4	3.92	8	49	32	21.6
Ms4beta16	4	3.94	16	49	32	21.6
Ms4beta32	4	3.94	32	49	32	21.6
Ms5beta4	5	4.91	4	49	32	21.6
Ms5beta8	5	4.92	8	49	32	21.6
Ms5beta16	5	4.92	16	49	32	21.6
Ms5beta32	5	4.94	32	49	32	21.6
mi200Ms2	2	2.16	16	200	48	21.4
mi200Ms3	3	2.98	16	200	64	21.4
mi200Ms4	4	3.94	16	200	48	21.4
mi200Ms5	5	4.92	16	200	48	21.4

Note. All the runs are initialized with $T_{i0} = T_{e0} = T_0 = 10^{-2} m_e c^2/k_{\mathrm{B}}$ and $c/\omega_{\mathrm{pe}} = 10$ cells.

tracked. The shock is set up by reflecting an upstream electron-proton plasma moving along the $-\hat{x}$ direction off a conducting wall at the leftmost boundary of the computational box ($x = 0$). The interplay between the reflected stream and the incoming plasma causes a shock to form, which propagates along $+\hat{x}$. In the simulation frame, the downstream plasma is at rest. The pre-shock magnetic field is initialized along the $\hat{y}$ direction perpendicular to the shock direction of propagation (i.e., we focus on the case of a "perpendicular" shock). Our 2D setup—with the magnetic field lying in the simulation plane—allows us to capture the physics of both electron (whistler) and proton (mirror and proton cyclotron) anisotropy-driven instabilities that are crucial for electron heating. In Paper I (see their Appendix A), we have shown that the electron heating physics cannot be properly captured by 1D simulations or by 2D simulations initialized with the field along $\hat{z}$, i.e., orthogonal to the simulation plane.

We vary the shock Mach number M_s (defined in Equation (3)) and the pre-shock plasma beta β_{p0} (defined in Equation (4)) as listed in Table 3, where we summarize the physical and numerical parameters of our shock simulations. The values of M_s and β_{p0} cover the regime of pre-shock conditions expected in galaxy cluster shocks.

We point out that, in setting up our simulations, we do not have direct control over the upstream velocity in the shock frame V_1 (which enters the definition of M_s), but only on the upstream velocity in the downstream frame V_0. In other words, we have no direct way of prescribing M_s. In order to obtain a given "target" Mach number M_s, we iteratively solve the Rankine–Hugoniot jump conditions and select the value of V_0 that corresponds to the chosen M_s. In the parameter regime covered by our simulations, because the protons in the immediate post-shock region retain a significant degree of anisotropy, we solve the Rankine–Hugoniot relations under the assumption of a 2D adiabatic index $\Gamma = 2$. It follows that the actual value of Mach number measured a posteriori in our simulations ($M_{s,\mathrm{meas}}$ in Table 3) may differ from the Mach number M_s targeted a priori. In practice, Table 3 shows that the two values differ by, at most, a few percent.

The pre-shock particles are injected at a "moving injector," which recedes from the wall in the $+\hat{x}$ direction at the speed of light (as the injector recedes from the wall, the simulation box also expands with time). For further numerical optimization, we allow the moving injector to periodically jump backward (i.e., in the $-\hat{x}$ direction), so that its distance ahead of the shock is always on the order of a few proton Larmor radii (see Paper I for details). The pre-shock particles are initialized as a drifting Maxwell-Jüttner distribution with a temperature $T_{i0} = T_{e0} = T_0 = 10^{-2} m_e c^2/k_{\mathrm{B}}$.[10] We resolve the electron skin depth c/ω_{pe} (defined in Equation (8)) with 10 computational cells, so that the electron Debye length is appropriately captured. We use a time resolution of $dt = 0.045\ \omega_{\mathrm{pe}}^{-1}$. The number of particles per cell N_{ppc} (including both species) is given in Table 3. Convergence checks, with regard to spatial resolution and number of particles per cell, have been performed in Paper I.

The shock structure is controlled by the proton Larmor radius

$$r_{\mathrm{Li}} = \frac{V_0}{v_{\mathrm{A}}}\sqrt{\frac{m_i}{m_e}}\ \frac{c}{\omega_{\mathrm{pe}}} \gg \frac{c}{\omega_{\mathrm{pe}}}, \tag{16}$$

where the Alfvén speed is $v_{\mathrm{A}} = B_0/\sqrt{4\pi m_i n_0}$. Similarly, the evolution of the shock occurs on a timescale given by the proton Larmor gyration period $\Omega_{\mathrm{ci}}^{-1} = r_{\mathrm{Li}} V_0^{-1} \gg \omega_{\mathrm{pe}}^{-1}$. The need to resolve the electron scales, and at the same time to capture the shock evolution for many $\Omega_{\mathrm{ci}}^{-1}$, is an enormous computational challenge for the realistic mass ratio $m_i/m_e = 1836$. Thus, we adopt a reduced mass ratio $m_i/m_e = 49$ for most of our runs, but we have tested that a higher mass ratio yields identical results (in Appendix A, we explore the dependence on Mach number of a few simulations with $m_i/m_e = 200$). In Paper I, we have argued that, for our reference shock with $M_s = 3$ and $\beta_{p0} = 16$, the efficiency of electron irreversible heating is nearly insensitive to the mass ratio, up to $m_i/m_e = 1600$. For $m_i/m_e = 49$, we choose the transverse size of the box L_y to be $\sim 150\ c/\omega_{\mathrm{pe}} \sim 21\ c/\omega_{\mathrm{pi}}$, which is sufficient to capture the growth of proton instabilities in the downstream.

5.2. Dependence on M_s

In this subsection, we compare the results of shock simulations with fixed $\beta_{p0} = 16$ and varying Mach number from $M_s = 2$ up to 5 (runs Ms2beta16, Ms3beta16, Ms4beta16, and Ms5beta16 in Table 3). We employ a reduced mass ratio of $m_i/m_e = 49$, but we show in Appendix A that identical results are obtained for a higher value of the mass ratio, $m_i/m_e = 200$.

Figure 7 shows the y-averaged profiles of various quantities in the shock at time $\Omega_{\mathrm{ci}} t = 22$, as a function of the x-coordinate relative to the shock location x_{sh}, in units of the proton Larmor

[10] Because we fix the thermal energy in units of the electron rest mass energy, it follows that different values of plasma beta are obtained by varying the ratio $\omega_{\mathrm{pe}}/\Omega_{\mathrm{ce}}$. In a few representative cases, we have verified that the two choices (i.e., varying $\omega_{\mathrm{pe}}/\Omega_{\mathrm{ce}}$ at fixed $k_{\mathrm{B}}T_0/m_e c^2$ or varying $k_{\mathrm{B}}T_0/m_e c^2$ at fixed $\omega_{\mathrm{pe}}/\Omega_{\mathrm{ce}}$) yield identical results, as long as the shock Mach number and the plasma beta are the same, and the electrons stay non-relativistic.

radius $r_{\rm Li}$ defined in Equation (16). Panel (a) shows the profiles of density (thick lines, see the legend in panel (d)) and magnetic field strength (thin lines with the same color coding as the thick lines). In agreement with the Rankine–Hugoniot relations, the density jump is larger for higher M_s. As a result of flux freezing alone, one would expect the magnetic field to be $B_{\rm ff} = (n/n_0)B_0$, i.e., its spatial profile should be identical to the density profile. The fact that the field strength $|B|$ in Figure 7(a) exceeds the expectation from flux freezing is to be attributed to magnetic fluctuations. Because the deviation is more pronouced at high M_s, whereas thin and thick lines overlap at low M_s, we expect from panel (a) that the strength of magnetic field fluctuations should increase with Mach number.

This is confirmed in Figure 8, where we present the 2D plots of $\delta B_x/B_{\rm ff}$ for the same simulations as in Figure 7. It is apparent that the strength of long-wavelength fluctuations steadily increases with Mach number (i.e., from top to bottom). Such waves—a combination of proton cyclotron modes and mirror modes—accompany the relaxation of the proton temperature anisotropy. As we have discussed in Section 4.1, protons are expected to be highly anisotropic in the immediate post-shock region, with a degree of anisotropy that scales as $T_{i,\perp}/T_{i,\parallel} \propto M_s^2$. The fact that shocks with higher M_s lead to stronger proton anisotropy has two consequences: (i) the larger amount of free energy in proton anisotropy can generate stronger proton waves, as is observed in Figures 8 and 7(a); (ii) as predicted by linear theory (see Appendix C), the waves grow faster for higher levels of anisotropy (ergo, higher M_s). In fact, Figure 8 shows that the peak of wave activity is located right at the shock for high Mach numbers ($M_s = 4$ and 5), and it shifts farther and farther downstream for lower and lower Mach numbers (it lies at $(x - x_{\rm sh})/r_{\rm Li} \sim -2.5$ for $M_s = 3$ and at $(x - x_{\rm sh})/r_{\rm Li} \lesssim -10$ for $M_s = 2$), due to the slower and slower wave growth.

For $M_s = 2$ and 3, the wave pattern in the shock ramp is dominated by short-wavelength electron whistler waves, rather than by the long-wavelength proton waves appearing for $M_s = 4$ and 5. In fact, the peak at $x \sim x_{\rm sh}$ in the green and blue lines of Figure 7(b) reflects the energy in whistler modes. For high Mach numbers, proton-driven modes are so strong that they dominate the wave energy right at the shock (orange and red curves in Figure 7(b)), hiding the presence of whistler waves in Figures 8(c), (d). Still, electron whistler modes remain active in the shock ramp (their pattern appears more clearly at higher mass ratios, where proton and electron scales are better separated, see Appendix A). There, they mediate efficient entropy production, as we discuss below.

As we have just described, the downstream proton waves are sourced by the proton anisotropy induced at the shock, which is expected to be stronger at higher M_s. This trend is confirmed in the peak anisotropy of Figure 7(d) (compare the curves at $x \sim x_{\rm sh}$), with the exception of the red curve of $M_s = 5$. Here, anisotropy-driven proton instabilities are so violent that the proton anisotropy is not even allowed to reach its expected peak. Due to pitch angle scattering by the proton cyclotron and mirror modes, the proton anisotropy is reduced below the marginal stability condition

$$\frac{T_{i,\perp}}{T_{i,\parallel}} - 1 \simeq \frac{1.1}{\beta_{i,\parallel}^{0.55}}, \tag{17}$$

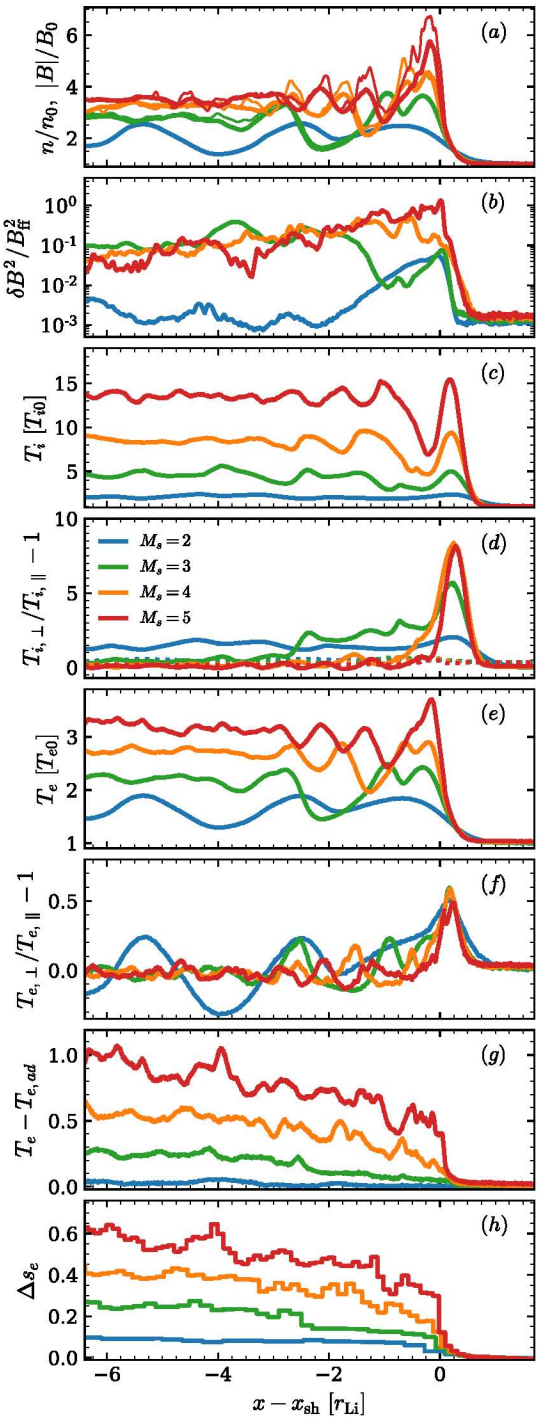

Figure 7. Dependence on M_s of various y-averaged quantities, from our shock simulations `Ms2beta16`, `Ms3beta16`, `Ms4beta16`, and `Ms5beta16`, at $t = 22\,\Omega_{\rm ci}^{-1}$ (the legend is in panel (d)). The x-coordinate (aligned with the shock direction of propagation) is measured relative to the shock location $x_{\rm sh}$, in units of the proton Larmor radius $r_{\rm Li}$. From top to bottom, we plot: (a) number density (thick lines) and magnetic field strength (thin lines); (b) energy in magnetic fluctuations, normalized to the energy of the frozen-in field; (c) mean proton temperature; (d) proton temperature anisotropy (with dotted lines representing the marginal stability threshold in Equation (17)); (e) mean electron temperature; (f) electron temperature anisotropy; (g) excess of electron temperature beyond the adiabatic prediction for an isotropic gas; (h) change in electron entropy. The efficiency of electron irreversible heating increases monotonically with M_s.

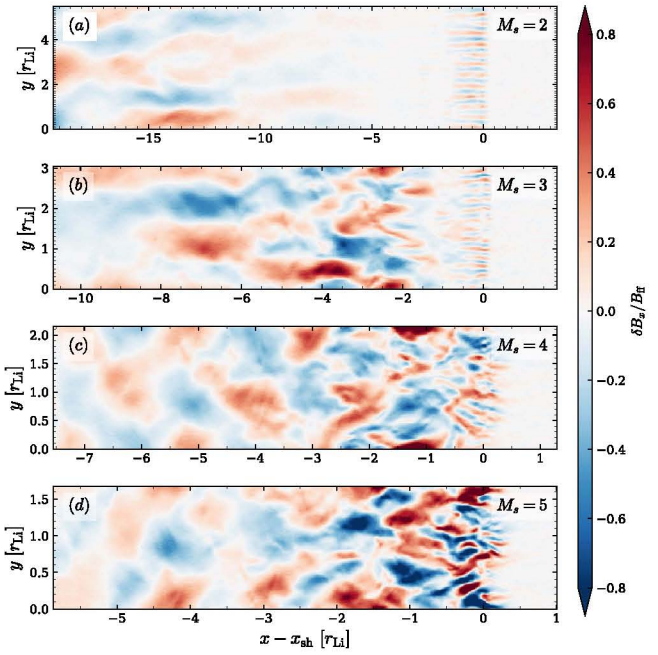

Figure 8. Dependence on M_s of the 2D structure of magnetic field fluctuations $\delta B_x/B_{ff}$ in the shock simulations `Ms2beta16`, `Ms3beta16`, `Ms4beta16`, and `Ms5beta16` at $t = 22\ \Omega_{ci}^{-1}$. The x-coordinate is measured relative to the shock location x_{sh}; both x and y coordinates are normalized to the proton Larmor radius r_{Li}. Notice that the x and y extents of the box are different for different M_s.

which is indicated with dotted lines in Figure 7(d). Because proton-driven waves are stronger for higher M_s, the relaxation toward the marginal stability threshold is faster for higher M_s, in analogy to what we discussed in Section 4.2. The case of $M_s = 2$, where proton modes are the weakest, is the only one where the degree of proton anisotropy remains significant (see the blue line in Figure 7(d) in the far downstream).

Given that protons in the far downstream are generally isotropic, their temperature can be properly quantified by the isotropic-equivalent estimate

$$T_i = \frac{2\,T_{i,\perp} + T_{i,\parallel}}{3}, \tag{18}$$

which we present in Figure 7(c). The trend seen in the plot, i.e., T_i/T_{i0} increasing with M_s, is driven by the fact that the temperature jump predicted by the Rankine–Hugoniot relations for the overall fluid is a monotonic function of M_s, in combination with the fact that most of the post-shock fluid energy resides in protons (rather than electrons or proton-driven modes). At sufficiently high Mach numbers, we then expect that $T_i/T_{i0} \propto M_s^2$ (i.e., as predicted by the Rankine–Hugoniot relations), a trend confirmed by Figure 7(c).

So far, we have mostly focused on the proton physics. With regard to electrons, we find that the post-shock electron temperature is a monotonically increasing function of M_s (Figure 7(e)). This might just follow from the dependence on M_s of the adiabatic heating efficiency, Because the density compression increases with M_s (Figure 7(a)).

However, we find that the efficiency of irreversible electron heating is also higher at larger M_s. In panel (h), we present the electron entropy profile as measured directly from our simulations using Equation (5), while in panel (g), we show the excess of electron temperature $T_e = (2\,T_{e,\perp} + T_{e,\parallel})/3$ beyond the adiabatic prediction appropriate for a 3D non-relativistic gas

$$\frac{T_{e,\mathrm{ad}}}{T_{e0}} = \left(\frac{n_e}{n_{e0}}\right)^{2/3}. \tag{19}$$

The fact that the efficiency of electron irreversible heating increases with Mach number can be promptly understood from the results obtained in Sections 3 and 4. First of all, the electron fluid suffers a faster compression while passing through the ramp of a high-M_s shock, as compared to a low-M_s shock. As we have shown in Section 3.2 (case A), this drives the electrons to larger levels of anisotropy, resulting in stronger whistler waves and faster rates of adiabatic breaking, which leads to more efficient entropy production. In addition, the highly anisotropic protons present in high-M_s shocks generate strong proton modes, as we have discussed in Section 4.2 (case B). The resulting field amplification provides another channel to induce electron anisotropy and ultimately leads to electron entropy increase. The stronger proton-driven modes at higher M_s result in higher efficiencies of irreversible electron heating (Section 4.2).

While the first mechanism (case A) is present for all the values of Mach number that we investigate, the second (case B) does not operate for $M_s = 2$. Here, the post-shock proton anisotropy is weak, and the strength of the resulting proton modes is insufficient to drive the electrons above the threshold of the whistler instability. In the absence of pitch angle scattering to break the adiabatic invariance, the electron entropy (blue line in Figure 7(h)) does not change behind the shock ramp (where entropy production is induced by compression, as in case A). The same was observed in Section 4.2.

In the shock with $M_s = 3$ (green line in panel (h)), case A controls the entropy increase in the shock ramp, whereas proton modes (ergo, case B) are responsible for the additional entropy jump seen at $(x - x_{sh})/r_{Li} \sim -2.5$. For $M_s = 4$ and 5 (orange and red curves, respectively), proton-driven modes grow fast, and the field amplification that they induce co-exists with the large-scale compression of the upstream field (i.e., case A and B are spatially coincident) in the shock ramp. This explains why most of the entropy increase for $M_s = 4$ and 5 is localized in the shock transition region. However, because the strength of proton modes remains significant for several proton Larmor radii behind the shock, the proton waves can occasionally excite local patches of electron anisotropy that exceed the whistler threshold. The resulting whistler activity can further increase the electron entropy downstream from the shock, in analogy to what we have discussed in Section 4.2.

5.3. Dependence on β_{p0}

In this subsection, we investigate the dependence of our results on plasma beta, at fixed Mach number. We vary β_{p0} from 4 up to 32, for two different values of Mach number: $M_s = 3$ in Section 5.3.1 and $M_s = 5$ in Section 5.3.2. We demonstrate that both choices of M_s lead to similar conclusions.

5.3.1. $M_s = 3$

Figure 9 compares the results of runs `Ms3beta4`, `Ms3beta8`, `Ms3beta16`, and `Ms3beta32` having a fixed Mach number $M_s = 3$. The density compression across the

shock is only weakly dependent on β_{p0} (Figure 9(a)), as expected from the Rankine–Hugoniot relations in the limit of high beta. Similarly, the Rankine–Hugoniot jump conditions justify why the post-shock proton temperature (Figure 9(c)) and the proton anisotropy at the shock (Figure 9(d) at $x \sim x_{\rm sh}$) are nearly insensitive to β_{p0}.

Given the relatively weak proton temperature anisotropy attained for $M_s = 3$ at the shock ($T_{i,\perp}/T_{i,\parallel} \sim 7$, panel (d)), proton-driven modes grow rather slowly in the downstream, and the magnetic field fluctuations in the shock ramp are powered by the electron whistler instability for all the values of β_{p0} we explore (see Figure 10 at the shock; electron whistler modes dominate the peak in magnetic energy seen in Figure 9(b) at the shock). In analogy to what we discussed in Section 4.3, the development of proton instabilities is faster at higher β_{p0} because the marginal stability threshold is lower (see Equation (17)), and thus easier to exceed, and because the growth rate is larger at higher β_{p0}, for a fixed degree of anisotropy. This explains why the magnetic energy in proton waves peaks closer to the shock at higher β_{p0} (in fact, it peaks at $(x - x_{\rm sh})/r_{\rm Li} \sim -3$ for the blue line of Figure 9(b), which refers to $\beta_{p0} = 4$, and at $(x - x_{\rm sh})/r_{\rm Li} \sim -2$ for the red line, which refers to $\beta_{p0} = 32$). From Figure 9(b), we also see that proton modes are stronger for higher β_{p0}, if normalized to the flux-frozen field. This is just a consequence of the fact that the free energy in proton anisotropy available to source the waves is larger for higher β_{p0}, when compared to the magnetic energy of the background field (the degree of anisotropy is β_{p0}-independent, but the proton thermal content obviously increases with β_{p0}).

Due to pitch angle scattering by the proton modes, the proton anisotropy drops at a faster rate for higher β_{p0} (Figure 9(d)), because the waves grow faster and are also stronger in this case. In the far downstream, the proton anisotropy settles to the marginal stability threshold of Equation (17), which is higher for lower β_{p0} (see the dotted lines in Figure 9(d)). It follows that low-β_{p0} shocks maintain an appreciable degree of proton anisotropy in the far downstream (see the blue line in Figure 9(d)). The fact that the resulting adiabatic index will be larger than the value $\Gamma = 5/3$ appropriate for a 3D isotropic gas (and so, the plasma will be less compressible) explains why the blue curve in the density profile of panel (a) lies below the other lines.

The adiabatic heating of electrons will follow the same trend as the density compression of panel (a). With regard to the efficiency of electron irreversible heating, we find that it displays a weak dependence on plasma beta (Figure 9(g) and (h)). From the findings in Sections 3.3 and 4.3, the lack of dependence on β_{p0} of the entropy prodution efficiency can be understood as a result of two competing effects. In the case that field amplification is induced by shock compression of the background field (case A), as appropriate for the shock ramp (for $M_s = 3$, proton waves grow farther downstream), higher values of β_{p0} generally lead to lower entropy production (Section 3.3). This is because, at higher β_{p0}, the electron whistler instability can be triggered at lower levels of temperature anisotropy (see the dependence on beta of the stability threshold in Equation (9)), a trend that is indeed seen at the shock in Figure 9(f). This leads to weaker whistler waves, less dramatic adiabatic breaking, and a slower rate of entropy production. In fact, in the ramp, shocks with lower β_{p0} tend to produce more entropy (see Figure 9(g) and (h) at $x \sim x_{\rm sh}$).

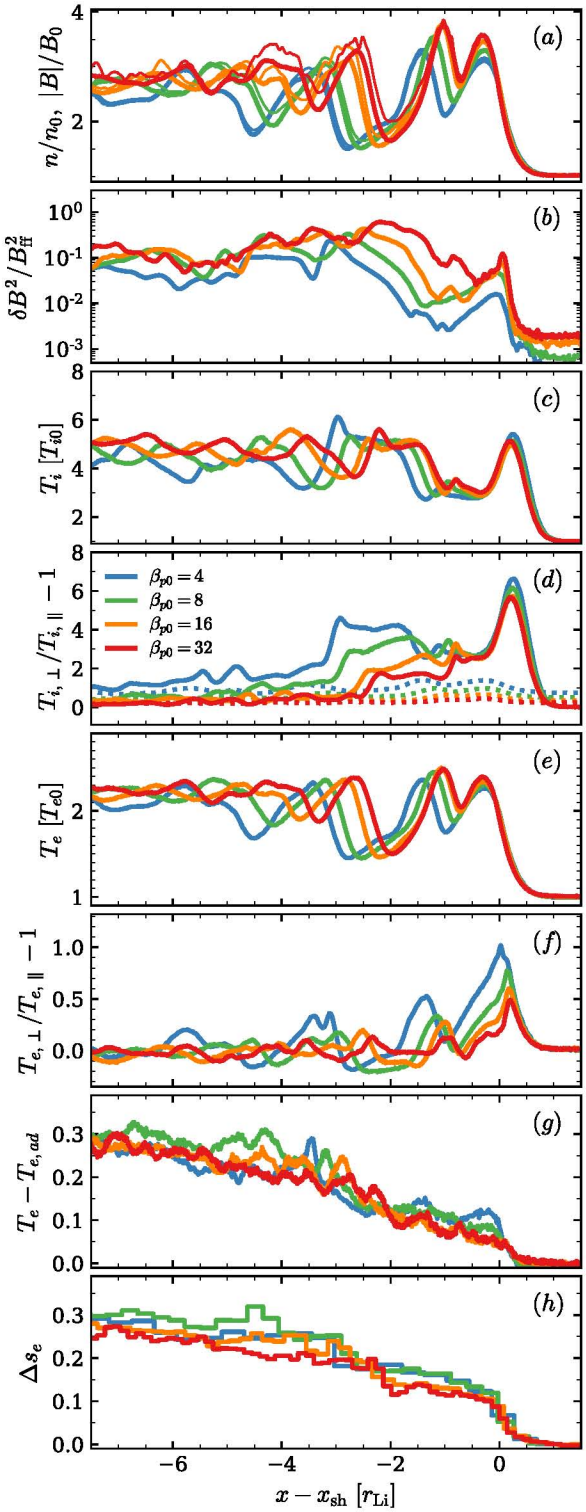

Figure 9. Dependence on β_{p0} of various y-averaged quantities in our shock simulations with $M_s = 3$ (runs `Ms3beta4`, `Ms3beta8`, `Ms3beta16`, and `Ms3beta32`), at $t = 20.7\ \Omega_{\rm ci}^{-1}$ (the legend is in panel (d)). See the caption of Figure 7 for details. Note that the increase in electron entropy is insensitive to the value of β_{p0}.

The trend is opposite when field amplification is induced by proton-driven waves (case B, see Section 4.3). In this case, higher values of β_{p0} lead to stronger proton modes (as observed

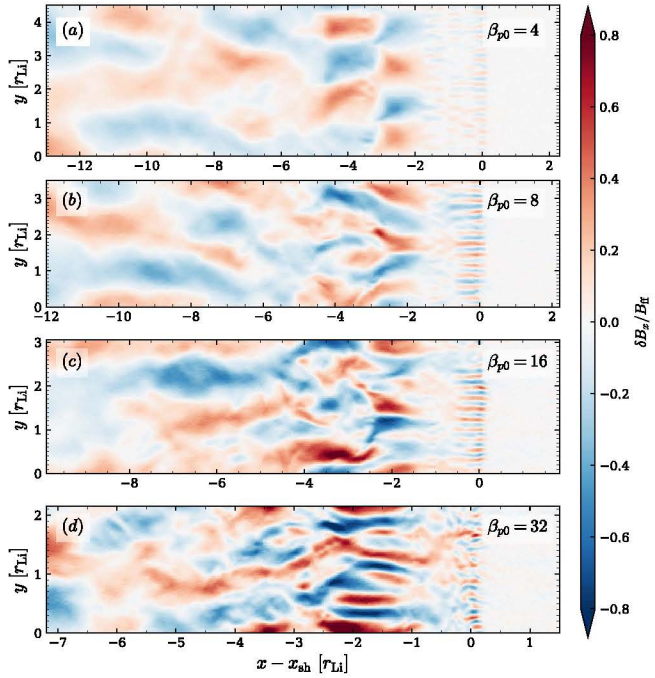

Figure 10. Dependence on β_{p0} of the 2D structure of magnetic field fluctuations $\delta B_x/B_{\rm ff}$ in the shock simulations `Ms3beta4`, `Ms3beta8`, `Ms3beta16`, and `Ms3beta32` at $t = 20.7\ \Omega_{\rm ci}^{-1}$. The x-coordinate is measured relative to the shock location $x_{\rm sh}$; both x and y coordinates are normalized to the proton Larmor radius $r_{\rm Li}$. Notice that the x and y extents of the box are different for different β_{p0}.

in Figure 9(b)), which perform more work onto the electrons, driving them further (and more often) into the unstable region of the whistler mode. In turn, this leads to more efficient entropy production at higher β_{p0}. This is the reason why, at $(x - x_{\rm sh})/r_{\rm Li} \sim -2.5$, i.e., at the peak of the energy in proton waves (see Figure 9(b)), the electron entropy jump is more pronounced for higher β_{p0}. It is here that shocks of high β_{p0}, which were lagging behind in electron entropy production, can catch up with low-β_{p0} shocks. The combination of the two opposite effects leads to an efficiency of electron irreversible heating that is nearly independent of β_{p0}, for $M_s = 3$.

5.3.2. $M_s = 5$

We now demonstrate that the same conclusion—i.e., the fact that the electron entropy production is independent of β_{p0}—also holds for shocks with $M_s = 5$, by showing (in Figure 11) the results of runs `Ms5beta4`, `Ms5beta8`, `Ms5beta16`, and `Ms5beta32`.

The main difference between $M_s = 5$ shocks and their $M_s = 3$ counterparts is that the proton anisotropy at the shock is now so large (Figure 11(d)) that proton waves grow quickly, and their energy peaks right at the shock (Figure 11(b)). This implies that the two competing effects mentioned above—i.e., the fact that shock compression leads to more entropy production in low-β_{p0} cases, whereas proton waves favor high-β_{p0} shocks—occur in the same spatial region (specifically, the shock ramp). Despite this difference from the $M_s = 3$ cases explored above, the electron entropy production in $M_s = 5$ runs still shows a negligible dependence on β_{p0} (panels (g) and (h)).

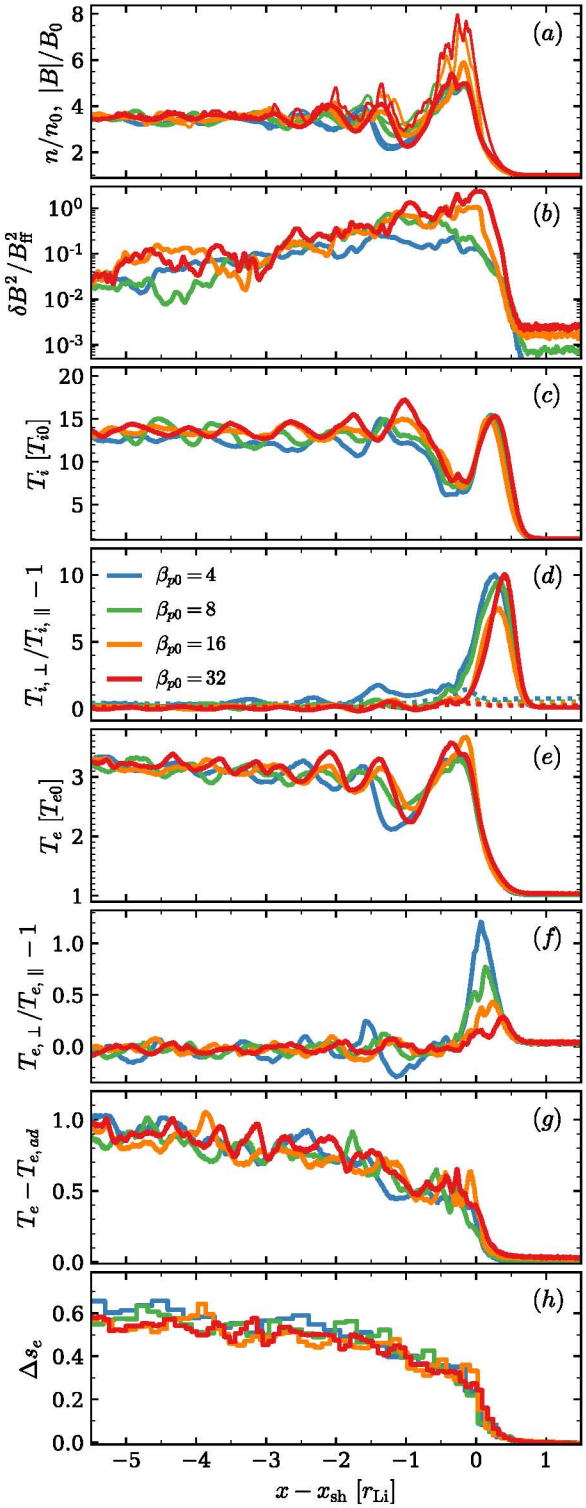

Figure 11. Dependence on β_{p0} of various y-averaged quantities in our shock simulations with $M_s = 5$ (runs `Ms5beta4`, `Ms5beta8`, `Ms5beta16`, and `Ms5beta32`), at $t = 22\ \Omega_{\rm ci}^{-1}$ (the legend is in panel (d)). See the caption of Figure 7 for details. Note that the increase in electron entropy is insensitive to the value of β_{p0}.

6. Key Results on Proton Anisotropy and Electron Heating

In this section, we summarize our shock results, combining the dependences on β_{p0} and M_s. The subscript "0" indicates quantities measured ahead of the shock, and "2" indicates quantities far downstream, computed by spatially averaging in

the region where the proton anisotropy has dropped below the threshold in Equation (17). We then time-average the spatial averages. In the runs with $M_s = 2$, where the proton anisotropy is yet to decrease below the threshold in Equation (17) even at times as large as $t = 40\ \Omega_{ci}^{-1}$, we compute the quantities with subscript "2" as spatial averages in the region at $(x - x_{sh})/r_{Li} \lesssim -20$. This particular choice of the averaging region is unlikely to affect our estimates for the efficiency of electron irreversible heating because proton waves are too weak to lead to appreciable entropy production in the far downstream; in fact, the only significant increase in electron entropy for $M_s = 2$ occurs at the shock ramp (see the blue line of Figure 7(h)). Our key results are shown in Figures 12 and 13 and summarized in Table 4.

Figure 12(a) presents the residual proton temperature anisotropy in the far downstream. As mentioned above, because $M_s = 2$ shocks have yet to relax to the threshold in Equation (17), our measurements are merely upper limits (as indicated by the arrows). For the other cases, we obtain a firm measurement of the proton anisotropy. We find that the residual proton anisotropy decreases with increasing β_{p0} (indicated by the colors, see the legend in panel (a)) and increasing M_s (indicated by the horizontal axis). These trends are properly captured by the dotted–dashed lines (with the same color coding as the symbols), which are obtained analytically as follows.

In analogy to the discussion in Section 4.1, we assume that the proton plasma can be described as a 2D gas in the immediate downstream region, with perpendicular temperature as in Equation (12) and parallel temperature as in Equation (13).[11] We also assume that the proton thermal content stays constant during the relaxation of the proton anisotropy. Even though protons convert part of their energy into magnetic fluctuations, the wave energy in the regime $\beta_{p0} \gg 1$ of interest here is much smaller than the proton thermal energy, so our assumption is satisfied. If we indicate (with T_{i2}) the isotropic-equivalent proton temperature, as in Equation (18) (which, as we said, stays the same during the relaxation of proton anisotropy), we can define the plasma beta in the far downstream as

$$\beta_{i2} \equiv \frac{8\pi n_2 T_{i2}}{B_2^2}, \tag{20}$$

where n_2 and B_2 are the density and field strength in the far downstream. There, proton waves have decayed and B_2 is the flux-frozen field strength, which can be determined via the shock density jump

$$\frac{B_2}{B_0} = \frac{n_2}{n_0} = r_{\mathrm{RH},\Gamma=5/3}, \tag{21}$$

where $\Gamma = 5/3$ is appropriate if the residual proton anisotropy is small in the far downstream, as in most of our cases. It follows that

$$\beta_{i2} = \frac{T_{i2}}{T_0}\frac{\beta_{p0}}{2}\frac{1}{r_{\mathrm{RH},\Gamma=5/3}}, \tag{22}$$

[11] The expression in Equation (12) assumes that electrons are heated adiabatically and that the energy in proton waves is much smaller than the proton thermal content. Both assumptions are reasonably satisfied in the parameter regime we explore.

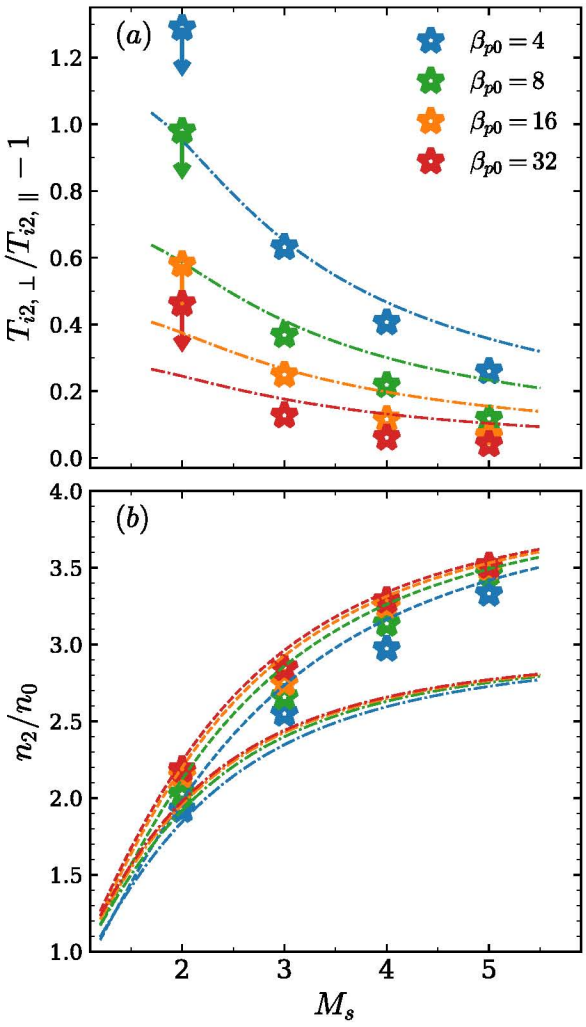

Figure 12. Time- and space-averaged downstream proton quantities from the shock simulations with $m_i/m_e = 49$ (listed in Table 3), as a function of Mach number M_s (on the horizontal axis) and plasma beta β_{p0} (as indicated by the colors; see the legend in the top panel). The data points in panel (a) represent the asymptotic proton temperature anisotropy. Dotted–dashed lines plot the predicted upper bound from Equation (23). The data points in panel (b) refer to the density compression. For comparison, we show the Rankine–Hugoniot density jump predictions for a 3D gas ($\Gamma = 5/3$, dashed lines) and a 2D gas ($\Gamma = 2$, dotted–dashed lines).

and the threshold in Equation (17), which we rewrite as

$$\frac{T_{i,\perp}}{T_{i,\parallel}} - 1 - \frac{1.1}{[3\beta_{i2}/(2\ T_{i,\perp}/T_{i,\parallel} + 1)]^{0.55}} \simeq 0, \tag{23}$$

may be solved for the anisotropy $T_{i2,\perp}/T_{i2,\parallel} - 1$ in the far downstream. The solutions of Equation (23) at different β_{p0} as a function of M_s are plotted as dotted–dashed lines in Figure 12(a). They capture the trend of decreasing asymptotic proton temperature anisotropy with increasing β_{p0} and M_s. Because Equation (17) (or equivalently, Equation (23)) sets an upper limit for the asymptotic proton anisotropy, it is also expected that our data points (apart from the $M_s = 2$ runs where the proton anisotropy is yet to relax) should lie below the upper bound prescribed by Equation (17).

Because the post-shock protons are not perfectly isotropic (Figure 12(a)), one might expect that the density jump n_2/n_0 from the upstream to the far downstream (Figure 12(b)) will lie

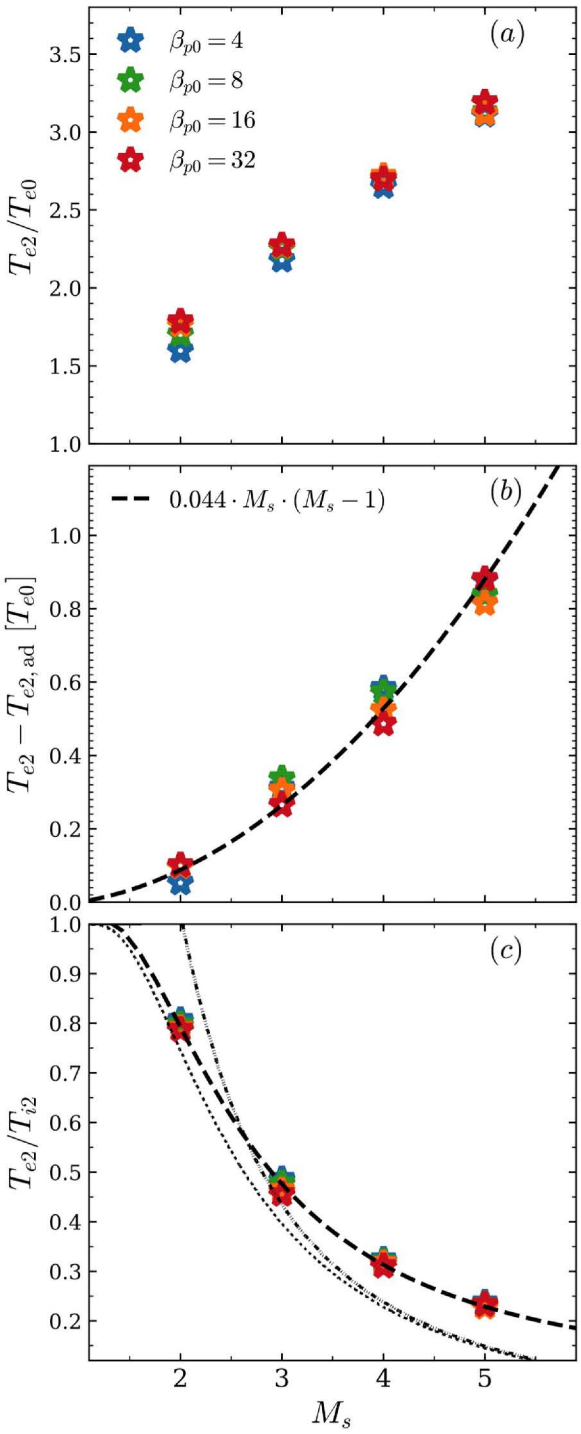

Figure 13. Time- and space-averaged downstream electron quantities from the shock simulations with $m_i/m_e = 49$ (listed in Table 3), as a function of Mach number M_s (on the horizontal axis) and plasma beta β_{p0} (as indicated by the colors, see the legend in the top panel). Panel (a) shows the total electron temperature jump across the shock. Panel (b) shows the electron temperature excess over the adiabatic expectation of a 3D gas. For comparison, a dashed black line shows our proposed fit of Equation (25). Panel (c) shows the post-shock electron-to-proton temperature ratio. For comparison, we show our prediction with a dashed black line (Equation (27)), the adiabatic expectation with a dotted line (Equation (27), but fixing $\Delta t_{e2,\rm irr} = 0$), and the scaling $T_{e2}/T_{i2} \propto M_s^{-2}$ with a dash–dotted line.

in between the predictions for a $\Gamma = 2$ gas (anisotropic, with two degrees of freedom) and for a $\Gamma = 5/3$ gas (perfecly isotropic, with three degrees of freedom). In panel (b), we plot the former with dotted–dashed lines and the latter with dashed curves. Indeed, our data points lie in between the two sets of curves. Because the post-shock protons tend to be more isotropic for higher β_{p0} and M_s (panel (a)), our data points in panel (b) tend to move closer to the $\Gamma = 5/3$ curves for either larger β_{p0} (compare the blue points for $\beta_{p0} = 4$ with the red points for $\beta_{p0} = 32$) or higher M_s (e.g., compare $M_s = 3$ with $M_s = 5$). The overall increase in n_2/n_0 with Mach number is simply a consequence of the Rankine–Hugoniot relations.

Next, we summarize (in Figure 13) the dependence on β_{p0} and M_s of the electron heating efficiency (the legend is in panel (a)). The overall electron temperature jump T_{e2}/T_{e0}, which includes both adiabatic and irreversible contributions, shows a weak dependence on β_{p0} and a systematic increase with M_s. In the regime of low Mach numbers investigated in this work, most of the electron temperature increase is contributed by adiabatic heating (compare the overall temperature jump in panel (a) with the irreversible contribution in panel (b)), so the temperature jump should be nearly equal to

$$T_{e2,\rm ad}/T_{e0} = (n_2/n_0)^{2/3} = r_{\rm RH,\Gamma=5/3}^{2/3} \tag{24}$$

as a result of density compression in a 3D gas. In fact, the mild increase in T_{e2}/T_{e0} with β_{p0} at fixed M_s is primarily a consequence of the dependence of n_2/n_0 on plasma beta (see Figure 12(b)).

At high values of M_s, the contribution of adiabatic heating will saturate, because $n_2/n_0 \to 4$ for a 3D gas. Here, most of the electron heating will be controlled by irreversible processes (i.e., associated with entropy increase). Panel (b) shows the efficiency of irreversible electron heating, quantified by the electron temperature increase beyond the adiabatic expectation. As discussed in Section 5, the efficiency of irreversible electron heating increases with Mach number and is nearly insensitive to plasma beta in the regime explored in this work (as a reminder, the fact that it is nearly independent of β_{p0} is due to the opposite effects of shock-compression and proton waves, which tend to cancel out). Combining all the data, we find that the efficiency of electron irreversible heating can be fitted quite well with the following simple function,

$$\frac{T_{e2} - T_{e2,\rm ad}}{T_{e0}} \simeq 0.044\, M_s\, (M_s - 1) \equiv \Delta t_{e2,\rm irr}, \tag{25}$$

with no appreciable dependence on β_{p0}. The above fitting function is shown in panel (b) with a dashed black line. Note that this fitting formula exhibits the correct behavior in the limit $M_s \to 1$: in the absence of a shock, the efficiency tends to zero.

Given our empirical fit in Equation (25), the overall electron temperature jump in the shock is given by

$$\frac{T_{e2}}{T_{e0}} = r_{\rm RH,\Gamma=5/3}^{2/3} + \Delta t_{e2,\rm irr}, \tag{26}$$

and the resulting ratio of electron and proton temperatures in the far downstream will be

$$\frac{T_{e2}}{T_{i2}} = \frac{r_{\rm RH,\Gamma=5/3}^{2/3} + \Delta t_{e2,\rm irr}}{2\,\Delta t_{\rm RH,\Gamma=5/3} - r_{\rm RH,\Gamma=5/3}^{2/3} - \Delta t_{e2,\rm irr}}, \tag{27}$$

where the proton temperature is obtained by subtracting the electron contribution from the Rankine–Hugoniot temperature jump $\Delta t_{\rm RH,\Gamma=5/3}$ of the overall fluid (assuming a 3D gas). This prediction is plotted in panel (c) with a black dashed line (we

Table 4
Key Results of the Shock Simulations with $m_i/m_e = 49$, as Discussed in Section 6

run name	M_s	β_{p0}	$T_{i2,\perp}/T_{i2,\parallel} - 1$	n_2/n_0	T_{e2}/T_{e0}	$(T_{e2} - T_{e2,\mathrm{ad}})/T_{e0}$	T_{e2}/T_{i2}
Ms2beta4	2	4	1.29	1.92	1.60	0.05	0.81
Ms2beta8	2	8	0.98	2.03	1.70	0.10	0.80
Ms2beta16	2	16	0.58	2.15	1.76	0.10	0.79
Ms2beta32	2	32	0.46	2.19	1.79	0.10	0.79
Ms3beta4	3	4	0.63	2.55	2.18	0.31	0.49
Ms3beta8	3	8	0.37	2.66	2.26	0.34	0.48
Ms3beta16	3	16	0.25	2.75	2.27	0.30	0.46
Ms3beta32	3	32	0.13	2.85	2.27	0.27	0.46
Ms4beta4	4	4	0.41	2.97	2.65	0.58	0.32
Ms4beta8	4	8	0.22	3.14	2.71	0.57	0.32
Ms4beta16	4	16	0.12	3.25	2.72	0.52	0.32
Ms4beta32	4	32	0.06	3.29	2.70	0.49	0.31
Ms5beta4	5	4	0.26	3.33	3.11	0.88	0.24
Ms5beta8	5	8	0.12	3.47	3.13	0.84	0.23
Ms5beta16	5	16	0.07	3.50	3.12	0.81	0.23
Ms5beta32	5	32	0.04	3.51	3.19	0.88	0.23

assume $\beta_{p0} = 32$ in calculating the Rankine–Hugoniot jump conditions, but the curve will be nearly the same as long as $\beta_{p0} \gg 1$). The prediction matches very well with the simulation results.

In Figure 13(c), we also compare our simulation results with the adiabatic expectation (dotted black line), which is obtained by assuming that electrons are heated only via adiabatic compression, without any entropy increase (i.e., we set $\Delta t_{e2,\mathrm{irr}} = 0$ in Equation (27)). In analogy to panel (b), the comparison of our data with the dotted curve shows that the efficiency of electron irreversible heating (and so, the deviation between our data and the adiabatic expectation) increases with shock Mach number. In Figure 13(c), we also plot the scaling $T_{e2}/T_{i2} \propto M_s^{-2}$ inferred from temperature ratio measurements behind the Earth and Saturn bow shocks (Schwartz et al. 1988; Masters et al. 2011; Ghavamian et al. 2013). Our results seem to follow this scaling, due to the combination of two effects: first, we find that in low Mach number shocks, most of the electron heating comes from adiabatic compression; second, in the absence of efficient electron entropy generation, the electron-to-proton temperature ratio is expected to scale as $T_{e2}/T_{i2} \simeq 8 \cdot 4^{2/3}/5\, M_s^2$ if $M_s \gtrsim$ a few (which we plot as a black dash–dotted line in panel (c)). In other words, we argue that the approximate $T_{e2}/T_{i2} \propto M_s^{-2}$ scaling observed at low Mach number shocks is primarily driven by adiabatic effects.[12]

We conclude with two important comments. First, we remark that the results of this section have been obtained for our reference value of the mass ratio, $m_i/m_e = 49$. In Paper I, we explicitly demonstrated that the electron entropy increase in our reference shock with $M_s = 3$ and $\beta_{p0} = 16$ is nearly insensitive to the mass ratio, from $m_i/m_e = 49$ up to $m_i/m_e = 200$ (see also Appendix A for the same conclusion in the case of $M_s = 5$ shocks with different β_{p0}). In addition, in Paper I we were able to extrapolate our results up to the realistic mass ratio, in controlled periodic box experiments meant to mimic the two possible scenarios for field amplification (i.e., shock-compression of the upstream field, or field amplification due to proton waves in the downstream). We found that the electron irreversible heating efficiency has only a weak dependence on mass ratio—less than a $\sim$30% decrease, as we increase the mass ratio from $m_i/m_e = 49$ up to $m_i/m_e = 1600$. Based on this result, we argue that the coefficient in Equation (25) should be reduced by the same fraction, $\sim$30%, for realistic mass ratios, so it will be $\simeq$0.03 instead of $\simeq$0.044.

Second, we remind the reader that our results have been obtained for strictly perpendicular shocks. In quasi-parallel shocks (i.e., where the angle between the pre-shock field and the shock direction of propagation is $\lesssim$45°), protons are expected to be efficiently reflected back upstream and accelerated via the Fermi process (e.g., Caprioli & Spitkovsky 2014; Park et al. 2015). In this regime, efficient electron heating (up to equipartition with the protons) was observed for supernova remnant conditions (i.e., at M_s of a few hundreds and $\beta_{p0} \sim 1$), and similar conclusions should apply in the low-M_s high-β_{p0} regime investigated here. In contrast, in quasi-perpendicular shocks, (i.e., where the angle between the pre-shock field and the shock direction of propagation is $\gtrsim$45°), protons are not efficiently injected into the Fermi process. At low M_s, electrons can still be efficiently accelerated, as we have shown in Guo et al. (2014a, 2014b). As long as the non-thermal electrons are energetically sub-dominant, we expect that the conclusions presented in this paper as regard to the electron heating efficiency will still apply for quasi-perpendicular field configurations.

7. Summary

In this paper, the second of a series, we have used 2D PIC simulations to quantify how the efficiency of electron heating and the post-shock electron-to-proton temperature ratio depend on the shock Mach number M_s and the plasma beta β_{p0}, in the regime relevant for galaxy cluster shocks. In Paper I, we described the physics of electron heating. In analogy to the so-called "magnetic pumping" mechanism (Spitzer & Witten 1953; Berger et al. 1958; Borovsky 1986), we found that two basic ingredients are needed for irreversible electron heating: (i) the presence of a temperature anisotropy, induced by field amplification coupled to adiabatic invariance; and (ii) a mechanism to break the adiabatic invariance itself. We found that the growth of whistler waves—triggered by the electron temperature anisotropy induced by field amplification

[12] We caution that our results cannot be directly compared to the available data from the Earth and Saturn bow shocks (where the $T_{e2}/T_{i2} \propto M_s^{-2}$ relation is observed) because the value of beta expected in these systems is lower (typically, $\beta_{p0} \sim 1$) than we explore in this work. We defer the investigation of electron heating in low Mach number shocks having $\beta_{p0} \sim 1$ to a later study.

—was responsible for the violation of adiabatic invariance, and for the efficient entropy production.

While Paper I focused only on a reference shock with $M_s = 3$ and $\beta_{p0} = 16$, here we have extended our study to a wide range of plasma beta ($4 \lesssim \beta_{p0} \lesssim 32$) and sonic Mach number ($2 \lesssim M_s \lesssim 5$). We first employed periodic box experiments to reproduce, under controlled conditions, the two mechanisms that can drive field amplification in shocks: (i) shock compression of the upstream field, and (ii) the growth of proton cyclotron modes accompanying the relaxation of proton temperature anisotropy. Armed with a detailed understanding of the electron heating efficiency in these two scenarios, and of its dependence on M_s and β_{p0}, we then studied the efficiency of electron entropy production in 2D shock simulations,[13] where the two mechanisms generally coexist.

Our main results are summarized in Section 6. Most importantly, we find that the irreversible electron heating efficiency in shocks is nearly independent of β_{p0}, and its dependence on M_s can be cast in a simple form: for our reference mass ratio $m_i/m_e = 49$, the post-shock electron temperature T_{e2} exceeds the adiabatic expectation $T_{e2,\rm ad}$ by an amount that scales with Mach number as $(T_{e2} - T_{e2,\rm ad})/T_{e0} \simeq 0.044\, M_s(M_s - 1)$, where T_{e0} is the pre-shock temperature (see Equation (25)). As discussed in Section 6, the coefficient should be reduced by ~30% when extrapolating to realistic mass ratios (so it will be ≃0.03 instead of ≃0.044). This can be used to predict the electron-to-proton temperature ratio in the shock downstream (see Equation (27)), with important implications for current and future measurements of electron-proton equilibration in galaxy cluster shocks.

Although we have only focused on perpendicular field geometries, we argue that our conclusions will also apply for quasi-perpendicular shocks (see Section 6), as long as the non-thermal electrons that are accelerated in such configurations stay energetically sub-dominant. For quasi-parallel geometries, protons are efficiently injected into the Fermi process, and the two species might be led to thermal equilibrium, as found by Park et al. (2015). The robustness of our electron heating mechanism—and the resulting efficiency of irreversible electron heating—in supernova remnant shocks (M_s of a few hundreds and $\beta_{p0} \sim 1$) and heliospheric shocks (low Mach number and $\beta_{p0} \sim 1$) remains to be explored.

This work is supported in part by the Black Hole Initiative at Harvard University through a grant from the Templeton Foundation. X.G. and R.N. acknowledge support from NASA TCAN NNX14AB47G and NSF grant AST 1312651. L.S. acknowledges support from DoE DE-SC0016542, NASA Fermi NNX-16AR75G, NASA ATP NNX-17AG21G, NSF ACI-1657507, and NSF AST-1716567. The simulations were performed on Habanero at Columbia, the BHI cluster at the Black Hole Initiative, NASA High-End Computing (HEC) Program through the NASA Advanced Supercomputing (NAS) Division at Ames Research Center, and NSF XSEDE resources (grant TG-AST080026N).

Appendix A
Dependence on the Mass Ratio

In this appendix, we investigate the dependence on M_s in shock simulations having $\beta_{p0} = 16$ and a higher value of the mass ratio ($m_i/m_e = 200$), as compared to the choice $m_i/m_e = 49$ employed in the main body of the paper (the runs presented in this appendix are `mi200Ms2`, `mi200Ms3`, `mi200Ms4`, and `mi200Ms5` in Table 3).

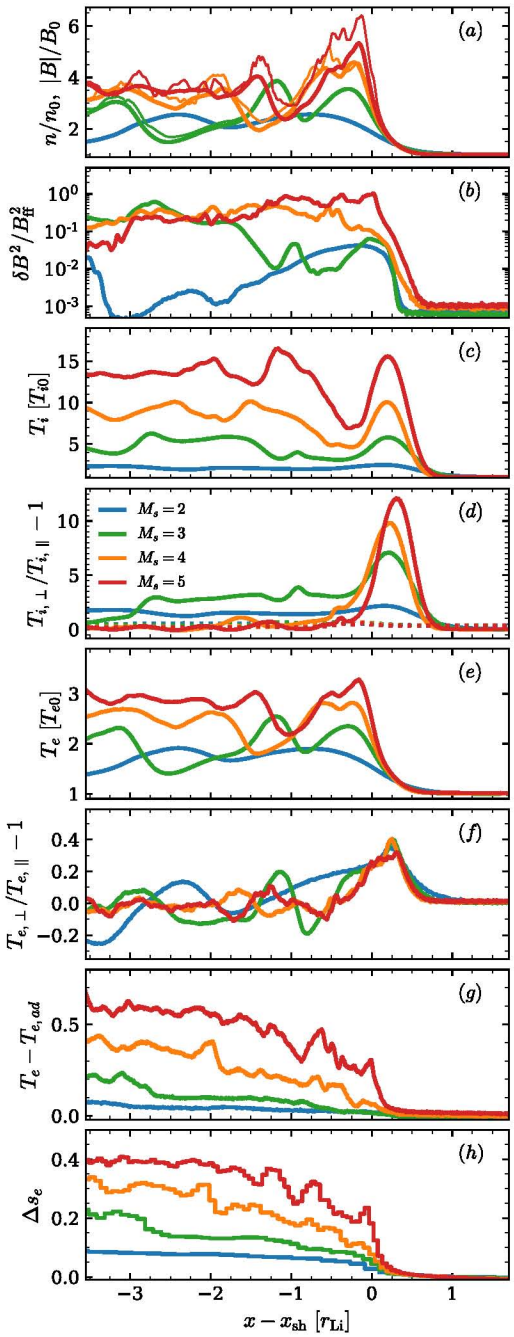

Figure 14. Dependence on M_s of various y-averaged quantities, from our shock simulations with $m_i/m_e = 200$ (`mi200Ms2`, `mi200Ms3`, `mi200Ms4`, and `mi200Ms5`), at $t = 12.9\ \Omega_{\rm ci}^{-1}$ (the legend is in panel (d)). The x-coordinate (aligned with the shock direction of propagation) is measured relative to the shock location $x_{\rm sh}$, in units of the proton Larmor radius $r_{\rm Li}$. From top to bottom, we plot: (a) number density (thick lines) and magnetic field strength (thin lines); (b) energy in magnetic fluctuations, normalized to the energy of the frozen-in field; (c) mean proton temperature; (d) proton temperature anisotropy (with dotted lines representing the marginal stability threshold in Equation (17)); (e) mean electron temperature; (f) electron temperature anisotropy; (g) excess of electron temperature beyond the adiabatic prediction for an isotropic gas; (h) change in electron entropy. If we compare to Figure 7, which employed a lower mass ratio ($m_i/m_e = 49$), we confirm that the shock physics (and in particular, the efficiency of electron irreversible heating) is nearly insensitive to the choice of mass ratio.

[13] In Paper I (see their Appendix A), we have shown that the electron heating physics cannot be properly captured by 1D shock simulations because they do not resolve the fastest growing mode of the electron whistler instability, whose wavevector is aligned with the large-scale field.

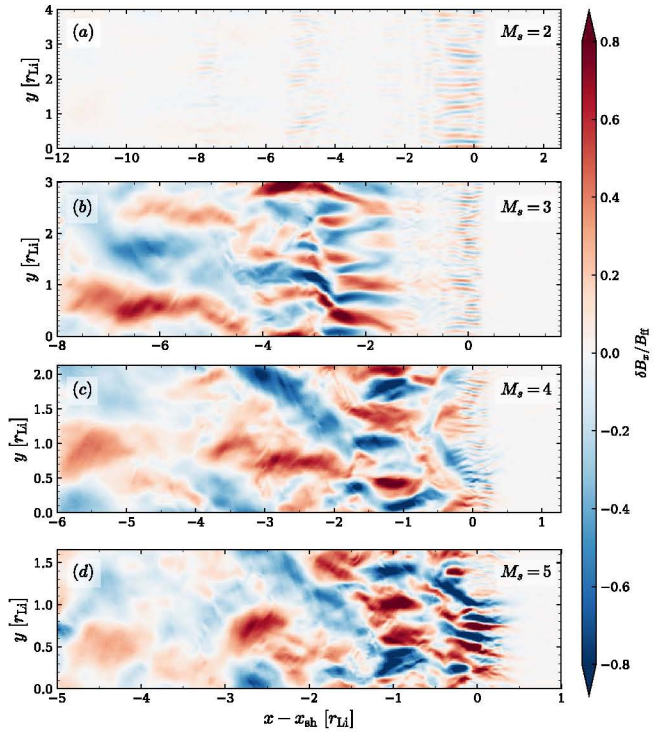

Figure 15. For $m_i/m_e = 200$, we present the dependence on M_s of the 2D structure of magnetic field fluctuations $\delta B_x/B_{ff}$ in the shock simulations `mi200Ms2`, `mi200Ms3`, `mi200Ms4`, and `mi200Ms5` at $t = 12.9\ \Omega_{ci}^{-1}$. The x-coordinate is measured relative to the shock location x_{sh}; both x- and y-coordinates are normalized to the proton Larmor radius r_{Li}. Notice that the x and y extents of the box are different for different M_s. As compared to Figure 8, which employed a lower mass ratio ($m_i/m_e = 49$), electron modes in the shock ramp now appear more clearly, due to the larger separation between electron and proton scales.

In Figure 14, we present the y-averaged profiles of various quantities at $t = 12.9\ \Omega_{ci}^{-1}$. Comparing with Figure 7 (which employed $m_i/m_e = 49$), we see that the profiles are almost identical for both protons and electrons. This proves that the electron heating physics is insensitive to the mass ratio, as long as proton and electron scales are sufficiently separated (see Paper I for further details on the dependence on mass ratio).

One important advantage of simulations with a higher mass ratio is the fact that electron whistler modes in the shock ramp appear more clearly for $m_i/m_e = 200$ (as compared to the case $m_i/m_e = 49$), due to the larger separation between electron and proton scales. This is particularly critical at high M_s because proton waves grow right at the shock and their wavelength is quite small (potentially approaching electron scales), due to the strong proton anisotropy (see Appendix C). For instance, electron whistler waves are much more apparent in Figure 15(c) (having $m_i/m_e = 200$) than in Figure 8(c) (which employed $m_i/m_e = 49$).

Appendix B
Linear Properties of the Electron Whistler Instability

According to our electron heating model, the presence of a mechanism to break the electron adiabatic invariance is essential for generating electron entropy. The electron whistler instability is usually invoked to serve this purpose in the shock downstream. In this appendix, we study the linear properties of the whistler instability that are useful for interpreting the simulation results presented in the main body of the paper.

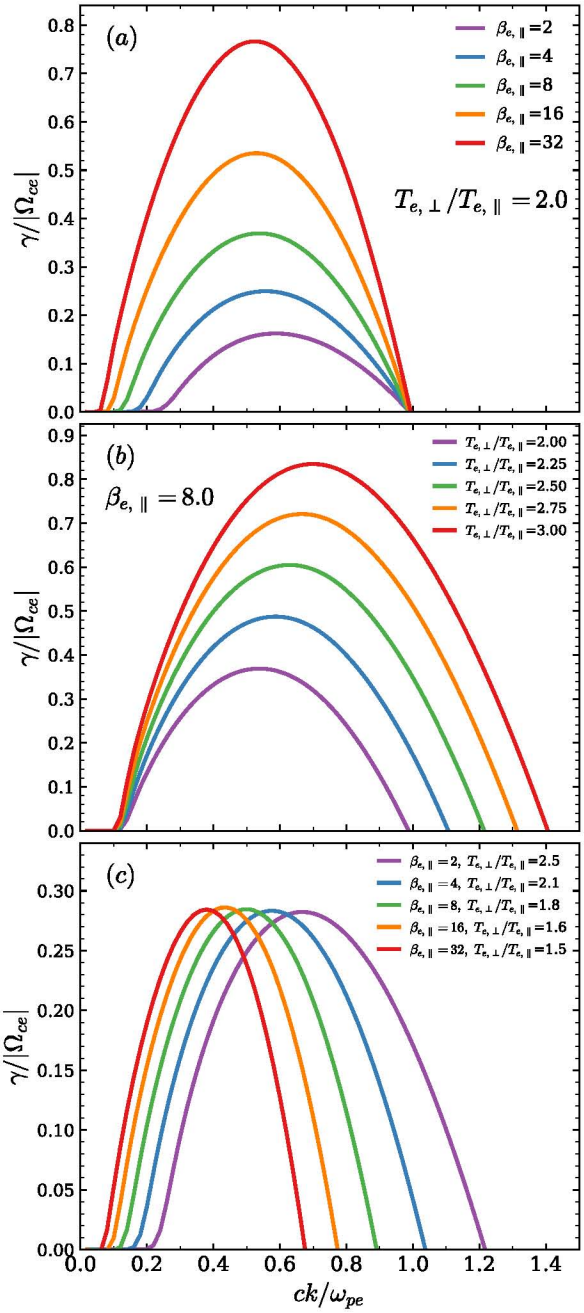

Figure 16. Dispersion relation of the electron whistler instability, i.e., the solution of Equation (28). Panel (a) shows the dependence on $\beta_{e,\parallel}$ at fixed electron temperature anisotropy $T_{e,\perp}/T_{e,\parallel} = 2$; panel (b) explores the dependence on temperature anisotropy at fixed $\beta_{e,\parallel}$; panel (c) shows the dispersion relation for different combinations of $\beta_{e,\parallel}$ and $T_{e,\perp}/T_{e,\parallel}$ that lead to a fixed maximum growth rate of $\gamma_{max} = 0.28\ \Omega_{ce}$.

Following Gary & Madland (1985), we solve the dispersion relation for the electron whistler instability

$$0 = D^{\pm}(k, \Omega)$$
$$= \Omega^2 - c^2k^2 + \omega_{pi}^2 \frac{\Omega}{kv_i} Z(\zeta_i^{\pm}) + \omega_{pe}^2 \frac{\Omega}{kv_{e,\parallel}^2} Z(\zeta_e^{\pm})$$
$$+ \omega_{pe}^2 \left(\frac{T_{e\perp}}{T_{e,\parallel}} - 1 \right) [1 + \zeta_e^{\pm} Z(\zeta_e^{\pm})], \quad (28)$$

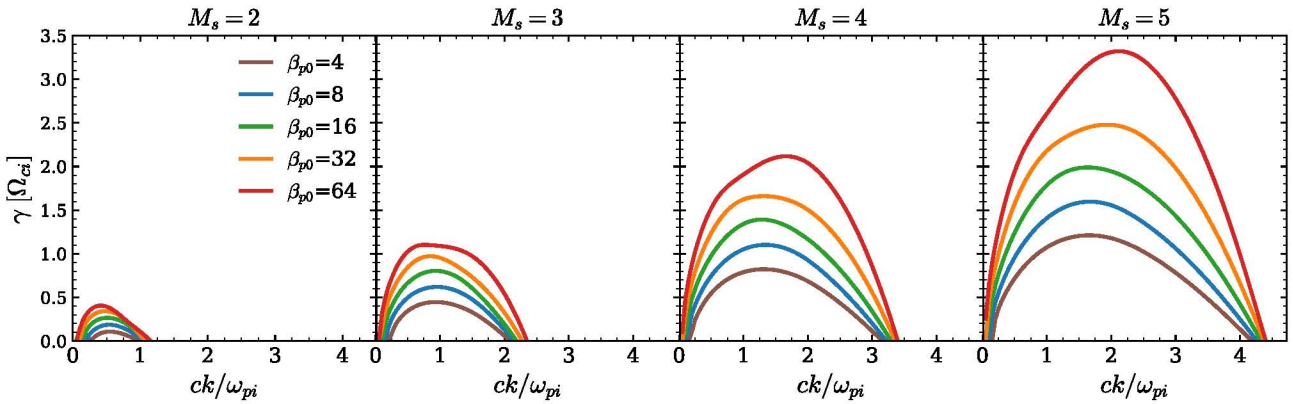

Figure 17. Dependence of the dispersion relation (growth rate γ as a function of wavevector k) of the proton cyclotron instability on the initial proton temperature anisotropy and plasma beta, phrased in terms of the shock Mach number M_s and the plasma beta β_{p0}. The relations of M_s and β_{p0} with the input parameters of the dispersion relation (i.e., $T_{i,\perp}/T_{i,\parallel}$, $T_{i,\parallel}$, T_e, β_e) can be derived as in Section 4.1.

where $\Omega = \omega + i\gamma$ is the frequency of the instability, k is the wavevector, $\zeta_e^{\pm} = (\Omega \pm \Omega_{ce})/kv_{e,\parallel}$, $\Omega_{ce} = (m_i/m_e)\Omega_{ci}$, $v_{e,\parallel} = (2\,k_B T_{e,\parallel}/m_e)^{1/2}$, $\zeta_i^{\pm} = (\Omega \pm \Omega_{ci})/kv_i$, $v_i = (2\,k_B T_i/m_i)^{1/2}$, and $Z(\zeta)$ is the plasma dispersion function

$$Z(\zeta) = \frac{1}{\sqrt{\pi}} \int_{-\infty}^{\infty} dx \frac{\exp(-x^2)}{x - \zeta}. \tag{29}$$

We explore how the dispersion relation of the electron whistler instability, i.e., its growth rate γ as a function of the wavevetor k, varies for different levels of electron temperature anisotropy $T_{e,\perp}/T_{e,\parallel}$, and of electron plasma beta parallel to the magnetic field $\beta_{e,\parallel}$. For all calculations, we fix $m_i/m_e = 49$ and $v_i = 0.02$ c.

Figure 16(a) compares the dispersion relation at fixed electron temperature anisotropy $T_{e,\perp}/T_{e,\parallel} = 2$ but different $\beta_{e,\parallel}$, ranging from 2 to 32. For a given temperature anisotropy, the growth rate of the electron whistler instability increases monotonically with $\beta_{e,\parallel}$, and the wavelength of the maximally growing mode increases—or equivalently, the wavevector of the maximally growing mode decreases. Figure 16(b) depicts the trend of the dispersion relation at fixed $\beta_{e,\parallel} = 8$, but for different levels of electron temperature anisotropy. We see that the growth rate of the electron whistler instability increases monotonically with increasing temperature anisotropy $T_{e,\perp}/T_{e,\parallel}$, and the wavelength of the maximally growing mode decreases. It follows that, in order to attain a given growth rate of the instability, the required temperature anisotropy is lower for higher $\beta_{e,\parallel}$. In addition, the wavelength of the maximally growing mode is longer at higher $\beta_{e,\parallel}$. Indeed, Figure 16(c) shows that, in order to reach a maximum growth rate of $\sim 0.28\ \Omega_{ce}$, the required temperature anisotropy decreases from 2.5 for $\beta_{e,\parallel} = 2$ to 1.5 for $\beta_{e,\parallel} = 32$. The maximally growing wave vector decreases from $0.7\ \omega_{pe}/c$ down to $0.35\ \omega_{pe}/c$.

Appendix C
Linear Properties of the Proton Cyclotron Instability

In our electron heating model, we require the presence of electron anisotropy. Electron anisotropy can be induced by field amplification via the proton cyclotron instability, which naturally occurs in the shock downstream, where it is sourced by proton anisotropy. In this appendix, we study the linear properties of the proton cyclotron instability and its dependence on plasma beta and on the level of proton temperature anisotropy.

Following Davidson & Ogden (1975), we solve the dispersion relation for the proton cyclotron instability (Equation (3) of Davidson & Ogden 1975)

$$\begin{aligned} 0 &= D^{\pm}(k, \Omega) \\ &= \Omega^2 - c^2k^2 + \omega_{pe}^2 \frac{\Omega}{k_y v_e} Z(\zeta_e^{\pm}) + \omega_{pi}^2 \frac{\Omega}{k v_{i,\parallel}^2} Z(\zeta_i^{\pm}) \\ &\quad - \omega_{pi}^2 \left(1 - \frac{T_{i\perp}}{T_{i,\parallel}}\right)[1 + \zeta_i^{\pm} Z(\zeta_i^{\pm})], \end{aligned} \tag{30}$$

where $\Omega = \omega + i\gamma$ is the frequency of the instability, k is the wavevector, and $\zeta_e^{\pm} = (\Omega \pm \Omega_{ce})/k_y v_e$, $v_e = (2\,k_B T_e/m_e)^{1/2}$, $\zeta_i^{\pm} = (\Omega \pm \Omega_{ci})/k_y v_{i,\parallel}$, $v_{i,\parallel} = (2\,k_B T_{i,\parallel}/m_i)^{1/2}$, and $Z(\zeta)$ form the plasma dispersion function

$$Z(\zeta) = \frac{1}{\sqrt{\pi}} \int_{-\infty}^{\infty} dx \frac{\exp(-x^2)}{x - \zeta}.$$

To calculate the dispersion relation from Equation (30), one possible choice for the set of parameters that we need to specify is $T_{i,\perp}/T_{i,\parallel}$, $T_{i,\parallel}$, T_e, β_e, m_i/m_e. As described in Section 4.1, in the immediate post-shock downstream, the values of $T_{i,\perp}/T_{i,\parallel}$, $T_{i,\parallel}$, T_e, β_e can be derived from M_s and β_{p0}. We adopt $m_i/m_e = 49$ for the computations presented here, but we have checked that the dispersion relation for $m_i/m_e = 1836$ is almost identical.

Figure 17 shows the results. We see that, with increasing M_s (as indicated from the titles of panels, from left to right), which leads to an increasing $T_{i,\perp}/T_{i,\parallel}$, both the maximum growth rate γ and the wavevector k of the fastest growing mode increase monotonically at fixed β_{p0}. At fixed proton temperature anisotropy $T_{i,\perp}/T_{i,\parallel}$ (i.e., fixed M_s), the growth rate and the wavevector of the fastest growing mode increase moderately with β_{p0} (as indicated by the different colors in each panel).

ORCID iDs

Xinyi Guo https://orcid.org/0000-0002-5425-9451

References

Akamatsu, H., Mizuno, M., Ota, N., et al. 2017, A&A, 600, A100
Basu, K., Sommer, M., Erler, J., et al. 2016, ApJL, 829, L23

Berger, J. M., Newcomb, W. A., Dawson, J. M., et al. 1958, PhFl, 1, 301
Birdsall, C. K., & Langdon, A. B. 1985, Plasma Physics via Computer Simulation (New York: McGraw-Hill)
Borovsky, J. E. 1986, PhFl, 29, 3245
Buneman, O. 1993, Computer Space Plasma Physics (Tokyo: Terra Scientific), 67
Caprioli, D., & Spitkovsky, A. 2014, ApJ, 783, 91
Chew, G. F., Goldberger, M. L., & Low, F. E. 1956, RSPSA, 236, 112
Davidson, R. C., & Ogden, J. M. 1975, PhFl, 18, 1045
Dieckmann, M. E., Bret, A., Sarri, G., et al. 2012, PPCF, 54, 085015
Eckert, D., Jauzac, M., Vazza, F., et al. 2016, MNRAS, 461, 1302
Erler, J., Basu, K., Trasatti, M., Klein, U., & Bertoldi, F. 2015, MNRAS, 447, 2497
Finoguenov, A., Sarazin, C. L., Nakazawa, K., Wik, D. R., & Clarke, T. E. 2010, ApJ, 715, 1143
Gary, S. P. 2005, GeoRL, 32, L13109
Gary, S. P., & Madland, C. D. 1985, JGRA, 90, 7607
Ghavamian, P., Schwartz, S. J., Mitchell, J., Masters, A., & Laming, J. M. 2013, SSRv, 178, 633
Guo, X., Sironi, L., & Narayan, R. 2014a, ApJ, 794, 153
Guo, X., Sironi, L., & Narayan, R. 2014b, ApJ, 797, 47
Guo, X., Sironi, L., & Narayan, R. 2017, arXiv:1710.07648
Hockney, R. W., & Eastwood, J. W. 1981, Computer Simulation Using Particles (New York: McGraw Hill)
Kale, R., Wik, D. R., Giacintucci, S., et al. 2017, MNRAS, 472, 940
Leroy, M. M. 1983, PhFl, 26, 2742
Lindner, R. R., Baker, A. J., Hughes, J. P., et al. 2014, ApJ, 786, 49
Markevitch, M. 2006, in ESA Special Publication 604, The X-ray Universe 2005, ed. A. Wilson (Paris: ESA), 723
Markevitch, M., Gonzalez, A. H., David, L., et al. 2002, ApJL, 567, L27
Masters, A., Schwartz, S. J., Henley, E. M., et al. 2011, JGRA, 116, A10107
Matsukiyo, S. 2010, PhPl, 17, 042901
Matsukiyo, S., & Scholer, M. 2003, JGRA, 108, 1
Ogrean, G. A., Brüggen, M., Röttgering, H., et al. 2013, MNRAS, 429, 2617
Park, J., Caprioli, D., & Spitkovsky, A. 2015, PhRvL, 114, 085003
Planck Collaboration, Ade, P. A. R., Aghanim, N., et al. 2013, A&A, 554, A140
Riquelme, M., Osorio, A., & Quataert, E. 2017, ApJ, 850, 113
Russell, H. R., Mcnamara, B. R., Sanders, J. S., et al. 2012, MNRAS, 423, 236
Russell, H. R., Sanders, J. S., Fabian, a. C., et al. 2010, MNRAS, 406, 1721
Schwartz, S. J., Thomsen, M. F., Bame, S. J., & Stansberry, J. 1988, JGR, 93, 12923
Sironi, L. 2015, ApJ, 800, 89
Sironi, L., & Narayan, R. 2015, ApJ, 800, 88
Spitkovsky, A. 2005, in AIP Conf. Proc. 801, Astrophysical Sources of High Energy Particles and Radiation, ed. T. Bulik, B. Rudak, & G. Madejski (Melville, NY: AIP), 345
Spitzer, J. L., & Witten, L. 1953, On the Ionization and Heating of a Plasma, Tech. Rep., NYO-999 (PM-S-6)
Spitzer, L. 1962, Physics of Fully Ionized Gases (New York: Wiley)
Trasatti, M., Akamatsu, H., Lovisari, L., et al. 2015, A&A, 575, A45
van Weeren, R. J., Röttgering, H. J. a., Brüggen, M., & Hoeft, M. 2010, Sci, 330, 347
Vink, J., Broersen, S., Bykov, A., & Gabici, S. 2015, A&A, 579, A13